Article

Cell Reports

Visual Experience-Dependent Oscillations and Underlying Circuit Connectivity Changes Are Impaired in *Fmr1* KO Mice

Graphical Abstract

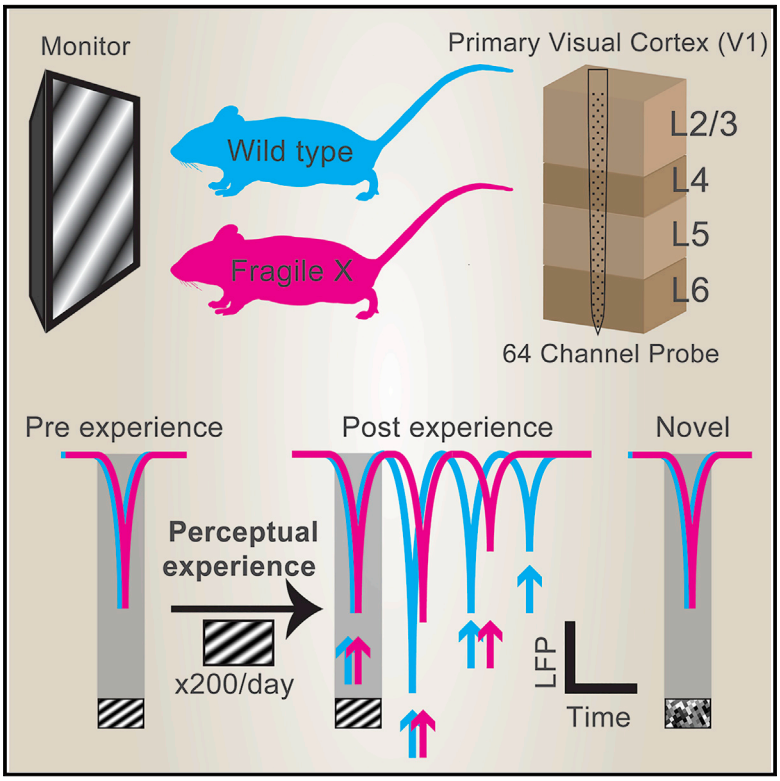

Authors

Samuel T. Kissinger, Qiuyu Wu, Christopher J. Quinn, Adam K. Anderson, Alexandr Pak, Alexander A. Chubykin

Correspondence

chubykin@purdue.edu

In Brief

Kissinger et al. study perceptual experience-dependent visual cortical oscillations in Fragile X mice using extracellular electrophysiology, revealing decreased oscillatory magnitudes and altered temporal profiles in Fragile X mice. Additionally, they perform a cross-layer functional connectivity analysis of these data and channelrhodopsin-2 assisted circuit mapping to identify underlying circuit differences.

Highlights

- Experience-dependent oscillations are reduced in magnitude and duration in FX mice
- A frequency shift is found in oscillations from FX mice
- Functional connections onto L4 FS cells are weaker in FX mice following experience
- L5 Pyr to L4 FS synapse is strengthened after experience in WT, but not in FX, mice

Kissinger et al., 2020, Cell Reports *31*, 107486
April 7, 2020
https://doi.org/10.1016/j.celrep.2020.03.050

CellPress

Cell Reports
Article

Visual Experience-Dependent Oscillations and Underlying Circuit Connectivity Changes Are Impaired in *Fmr1* KO Mice

Samuel T. Kissinger,[1,3] Qiuyu Wu,[1,3] Christopher J. Quinn,[2] Adam K. Anderson,[1] Alexandr Pak,[1] and Alexander A. Chubykin[1,4,*]
[1]Department of Biological Sciences, Purdue Institute for Integrative Neuroscience, Purdue University, West Lafayette, IN 47907, USA
[2]Department of Industrial Engineering, Purdue University, West Lafayette, IN 47907, USA
[3]These authors contributed equally
[4]Lead Contact
*Correspondence: chubykin@purdue.edu
https://doi.org/10.1016/j.celrep.2020.03.050

SUMMARY

Fragile X syndrome (FX), the most common inherited form of autism and intellectual disability, is a condition associated with visual perceptual learning deficits. We recently discovered that perceptual experience can encode visual familiarity via persistent low-frequency oscillations in the mouse primary visual cortex (V1). Here, we combine this paradigm with a multifaceted experimental approach to identify neurophysiological impairments of these oscillations in FX mice. Extracellular recordings reveal shorter durations, lower power, and lower frequencies of peak oscillatory activity in FX mice. Directed information analysis of extracellularly recorded spikes reveals differences in functional connectivity from multiple layers in FX mice after the perceptual experience. Channelrhodopsin-2 assisted circuit mapping (CRACM) reveals increased synaptic strength from L5 pyramidal onto L4 fast-spiking cells after experience in wild-type (WT), but not FX, mice. These results suggest differential encoding of visual stimulus familiarity in FX via persistent oscillations and identify circuit connections that may underlie these changes.

INTRODUCTION

Fragile X syndrome (FX) is the most common monogenetic inheritable form of intellectual disability (Gallagher and Hallahan, 2012). FX patients have high comorbidity with autism spectrum disorders (ASDs) (Hall et al., 2008; Harris et al., 2008) and exhibit learning impairments (Berry-Kravis, 2014). Several deficits in perception and learning have been found using visual tasks to assess human individuals with FX, suggesting the presence of neural dysfunction in the visual system associated with the loss of fragile X mental retardation protein (FMRP) expression (Farzin et al., 2008, 2011; Freund and Reiss, 1991; Gallego et al., 2014). Although the precise causes of these impairments are unclear, studies in *Fmr1* knockout (KO) mice have revealed diverse neurophysiological phenotypes associated with FMRP loss.

Morphologically, immature, excessive, and unstable dendritic spines were reported from both postmortem patient samples and FX animal models (Portera-Cailliau, 2012). Impaired synaptic plasticity has also been reported, including exaggerated metabotropic glutamate receptor (mGluR)-dependent long-term depression (LTD) (Bhattacharya et al., 2012; Hou et al., 2006; Huber et al., 2002; Nosyreva and Huber, 2006) and deficient cortical long-term potentiation (LTP) (Koga et al., 2015; Larson et al., 2005; Martin et al., 2016). Aberrant persistent activity in the somatosensory cortex and increased excitatory to inhibitory (E/I) ratios were found, consistent with a widely held theme that circuits are hyperexcitable in FX (Gibson et al., 2008; Hays et al., 2011). Recent work supports the notion that an E/I imbalance in autism is driven by decreased inhibition via parvalbumin positive (PV+) interneurons, though this may represent a compensatory mechanism designed to maintain peak depolarization rather than enhance it (Antoine et al., 2019). Two-photon calcium imaging studies have also revealed decreased activity of PV+ interneurons in the primary visual cortex (V1) of adult FX mice, as well as over-synchronized neural activity in the developing somatosensory cortex of young FX mice (Goel et al., 2018; Gonçalves et al., 2013).

These studies have been invaluable for revealing fundamental neurophysiological impairments in individual neurons and defined cortical layers of FX mice. To add to this work and to our understanding of visual impairments in FX, we characterized cross-layer neural activity in V1 of awake *Fmr1* KO mice that is modulated by perceptual experience. The recognition of familiar stimuli and their prominent physical features is a critical function of the visual system that is driven by learning. We recently discovered that visually evoked persistent low-frequency oscillations in both single units and local field potentials (LFPs) can encode visual familiarity in V1 of mice (Kissinger et al., 2018). These oscillations emerge after several days of perceptual experience and are not elicited by stimuli with novel spatial frequencies. Here, we ascertained the activity profile of these oscillations in FX mice as a readout of perceptual learning in V1 and sought to identify resulting changes in circuit connectivity and synaptic plasticity in FX mice and wild-type (WT) controls.

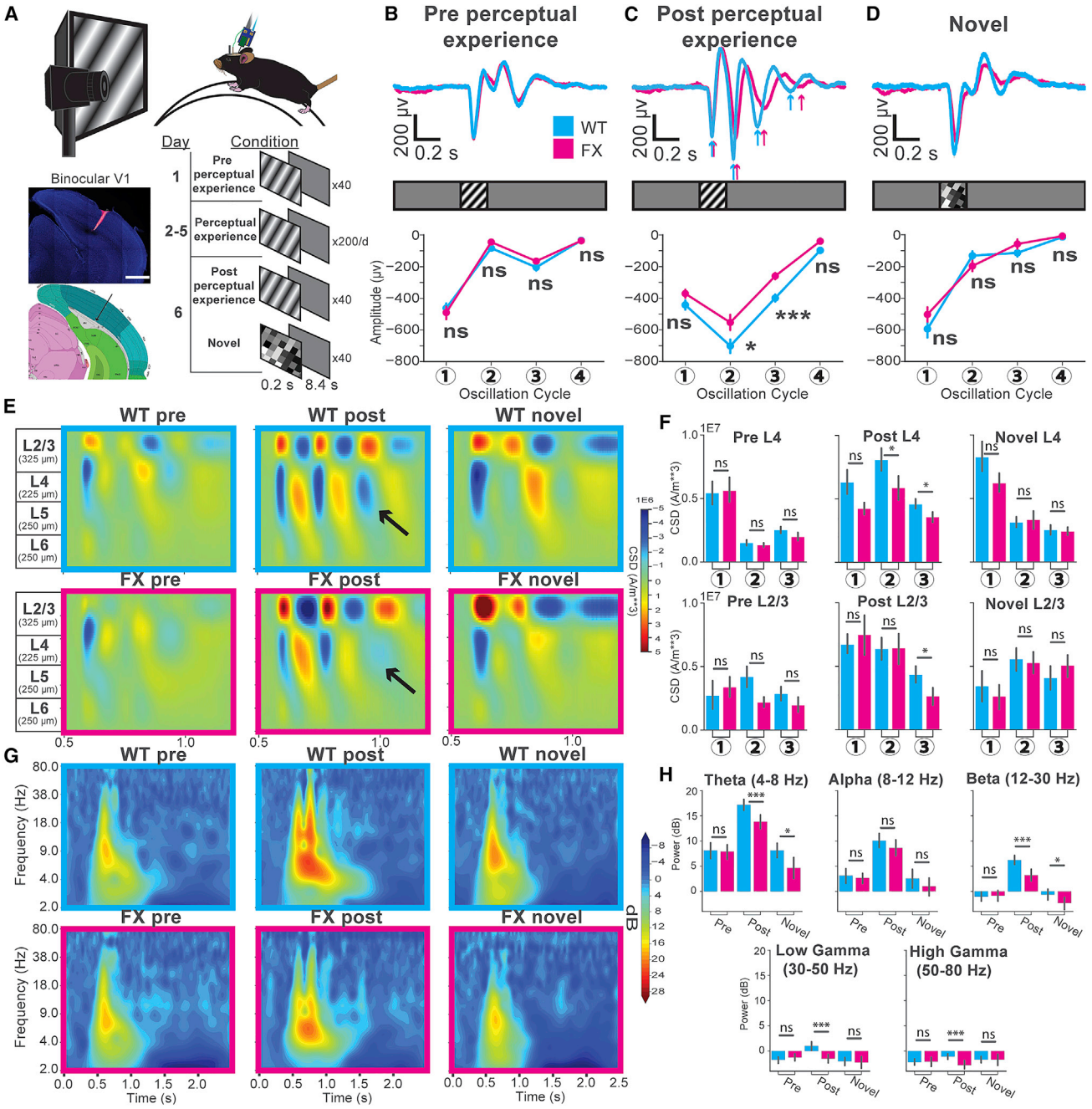

Figure 1. Attenuated Amplitude of Visually Evoked Oscillations in FX Mice

(A) Experimental setup for awake, head-fixed mice. The tiled composite confocal image shows the electrode track in V1 (blue, DAPI; red, Vybrant DiD dye; scale bar, 1,000 µm) compared to the 2019 Allen Institute for Brain Science mouse atlas. Available from https://mouse.brain-map.org/.

(B) Top: layer 4 visually evoked potentials (VEPs) in WT (cyan) and FX (magenta) mice before perceptual experience. Bottom: averaged amplitudes at 4 oscillation cycles. WT n = 37 trial averaged VEPs across 37 mice; FX n = 28 trial averaged VEPs across 28 mice. Linear mixed model (LMM) analysis: genotype: $F_{1, 64} = 0.17$; p = 0.681. Oscillation no.: $F_{3,192} = 235.97$; p < 1E−4. Genotype/oscillation no. interaction: $F_{3,192} = 1.04$; p = 0.376. Least square (LS) means test (Bonferroni corrected): cycle(1): estimate: 0.42; t(240) = 0.32; p = 1.0. (2): estimate: −0.54; t(240) = −1.21; p = 0.88. (3): estimate: −0.39; t(240) = −0.87; p = 1.0. (4): estimate: 0.34; t(240) = 0.76; p = 1.0. Standard error (SE): 0.45. Error bars indicate SEM. *p < 0.05; **p < 0.01; ***p < 0.001; ****p < 0.0001.

(C) Post-perceptual experience VEPs. LMM analysis: genotype: $F_{1,66} = 13.34$; p = 5E−4. Oscillation no.: $F_{3,198} = 234$; p < 1E−4. Genotype/oscillation no. interaction: $F_{3,198} = 2.44$; p = 0.06. LS means test (Bonferroni corrected): cycle(1): estimate: −0.79; t(199.6) = −1.56; p = 0.47. (2): estimate: −1.45; t(199.6) = −2.87; p = 0.018. (3): estimate: −2.16; t(199.6) = −4.26; p < 4.0E−4. (4): estimate: −0.80; t(199.6) = −1.59; p = 0.45. SE: 0.51.

(legend continued on next page)

We found that these oscillations were lower in power and shorter in duration in FX mice, suggesting attenuated encoding of familiar stimuli in V1. The timing of each oscillatory cycle was also delayed in FX mice, demonstrating that not only the power but also the temporal profile of this familiarity response is altered. Multiple functional connections between cortical layers were weaker in FX mice after perceptual experience, the most prominent of which were connections from multiple layers onto layer 4 (L4) fast-spiking (FS) cells and from L6 FS cells onto L2/3 and L4. Connection-specific changes in synaptic strength elicited by perceptual experience were impaired in FX mice, particularly at the L5 regular-spiking (RS) to L4 FS connection. Together, these results infer connections in V1 that may be involved in visual experience-dependent oscillations and suggest that impairments in these connections may underlie attenuation of the oscillations in FX mice.

RESULTS

Attenuated Visually Evoked Oscillations in LFPs in FX Mice

To determine differences in perceptual experience-dependent oscillatory activity in V1 of FX (*Fmr1* KO) mice, we subjected awake 2-month-old mice to a passive visual perceptual experience paradigm. Sinusoidal drifting gratings (0.2 s duration; spatial frequency = 0.03 cycles per degree of visual angle [cpd]; temporal frequency = 3 Hz; speed = 100 deg/s) were presented to the mice before and after passively viewing this stimulus 200 times/day over 4 days (inter-trial interval = 8.2 s; Figure 1A). Silicon probes (64 channels) were inserted normal to the surface of binocular V1 to record electrophysiological activity across all cortical layers while mice viewed full-field visual stimuli directly in front of them (Shobe et al., 2015). We simultaneously recorded pupil size and locomotion to assess arousal levels and to control for gain modulatory effects caused by locomotion. Visually evoked potentials (VEPs) were identified from layer 4 of V1 by taking the first and strongest negative deflection in LFPs occurring after visual stimulation. We first analyzed VEPs from trials where the mice did not run (immobile trials) to assess visually evoked activity in FX mice without any confounding effects of locomotion (Figure 1). Visually evoked responses before perceptual experience were comparable between naive wild-type (WT) and FX mice, characterized by a stimulus-locked VEP and occasionally followed by low-power oscillatory activity (Figure 1B). Perceptual experience induced persistent low-frequency oscillatory activity in both WT and FX mice, but these oscillations were significantly lower in amplitude in FX mice at the 2nd and 3rd cycles (Figure 1C). After perceptual experience, a subset of mice was presented a novel checkerboard stimulus that evoked stimulus-locked responses reminiscent of the pre condition. No significant differences in amplitude could be found in responses to novel stimuli between WT and FX mice (Figure 1D). The finding that stimulus-locked VEP amplitudes are comparable between WT and FX mice suggests that feedforward input to L4 is of similar strength. However, the oscillations persisting beyond the stimulus (which are strengthened by experience) are impaired in FX mice.

We estimated the translaminar currents underlying the oscillations across the cortical depth by performing current source density (CSD) analysis on the averaged LFPs across mice for each stimulus condition (Aizenman et al., 1996; Łeski et al., 2007; Mitzdorf, 1985; Pettersen et al., 2006; Figures 1E and 1F). Consistent with our previous findings, oscillatory activity was most prominently displayed in the superficial layers (L4 and L2/3), though it was observable across the cortical depth (Kissinger et al., 2018). The L4 current sinks were significantly stronger in WT mice after perceptual experience at the second and third oscillation cycles, with the third sink barely distinguishable in FX mice (Figures 1E and 1F, black arrows). The corresponding sinks in L2/3 at cycles 2 and 3 appeared stronger in FX mice but did not reach statistical significance. However, the L2/3 sink at cycle 3, similar to L4, was significantly attenuated in FX mice compared to WT. No significant differences in CSD could be found between WT and FX mice in either the pre or novel conditions (Figures 1E and 1F). To reveal any frequency-band-specific differences in the persistent (occurring after the stimulus; 0.7–1.2 s) oscillations between WT and FX mice, we quantified oscillatory power relative to the baseline period across a range of frequencies. This time-frequency analysis revealed no significant differences in the power of any frequency bands before perceptual experience between WT and FX mice (Figures 1G and 1H). However, the theta (4–8 Hz), beta (12–30 Hz), low gamma (30–50 Hz), and high gamma (50–80 Hz) frequency bands showed significantly lower power in FX mice after perceptual experience (Figures 1G and 1H). Although alpha (8–12 Hz) power was also lower in FX mice compared to WT, this decrease did not reach statistical significance. Mild differences were found in response to novel stimuli, with significantly higher

(D) Novel VEPs. LMM analysis: genotype: $F_{1,37} = 0.60$; p = 0.44. Oscillation no.: $F_{3,111} = 154$; p < 1E−4. Genotype/oscillation no. interaction: $F_{3,111} = 1.04$; p = 0.38. LS means test (Bonferroni corrected): cycle(1): estimate: −0.96; t(124.6) = −1.44; p = 0.61. (2): estimate: 2.42E−4; t(124.6) = 0.00; p = 1.0. (3): estimate: 0.29; t(124.6) = 0.44; p = 1.0. (4): estimate: −0.70; t(124.6) = −1.06; p = 1.0. SE: 0.66.

(E) Current source density (CSD) for LFPs across layers from the mice in (B), (C), and (D). The black arrows point to the third current sink in L4.

(F) Quantification of the CSD shown in (E). Mann-Whitney U test WT versus FX: layer 4: pre, sink1: t = 301; p = 0.47. sink2: t = 297; p = 0.44. sink3: t = 224; p = 5.79E−2. Post, sink1: t = 233; p = 0.06. sink2: t = 203; p = 1.72E−2. sink3: t = 221; p = 3.87E−2. Novel, sink1: t = 157; p = 0.20. sink2: t = 183; p = 0.46. sink3: t = 178; p = 0.40. Layer2/3: pre, sink1: t = 237; p = 0.09. sink2: t = 230; p = 0.07. sink3: t = 243; p = 0.11. Post, sink1: t = 267; p = 0.19. sink2: t = 295; p = 0.37. sink3: t = 199; p = . Post L2/3, sink3: t = 199; p = 1.41E−2. Novel, sink1: t = 177; p = 0.39. sink2: t = 180; p = 0.42. sink3: t = 147; p = 0.13.

(G) Time-frequency spectrograms from the layer 4 VEPs (from B, C, and D) for each condition.

(H) Oscillatory power across various frequency bands of the layer 4 VEPs. Mann-Whitney U test; pre: theta: t = 503, p = 0.33; alpha: t = 462, p = 0.16; beta: t = 525, p = 0.44; low gamma, t = 470, p = 0.19; high gamma, t = 508, p = 0.35. Post: theta: t = 304, p = 4.62E−4; alpha: t = 472, p = 0.10; beta: t = 270, p = 9.53E−5; low gamma: t = 278, p = 1.4E−4; high gamma t = 305, p = 4.83E−4. Novel: theta: t = 105, p = 0.01; alpha: t = 160, p = 0.22; beta: t = 122, p = 0.03; low gamma: t = 174, p = 0.36.

See also Figures S7 and S8.

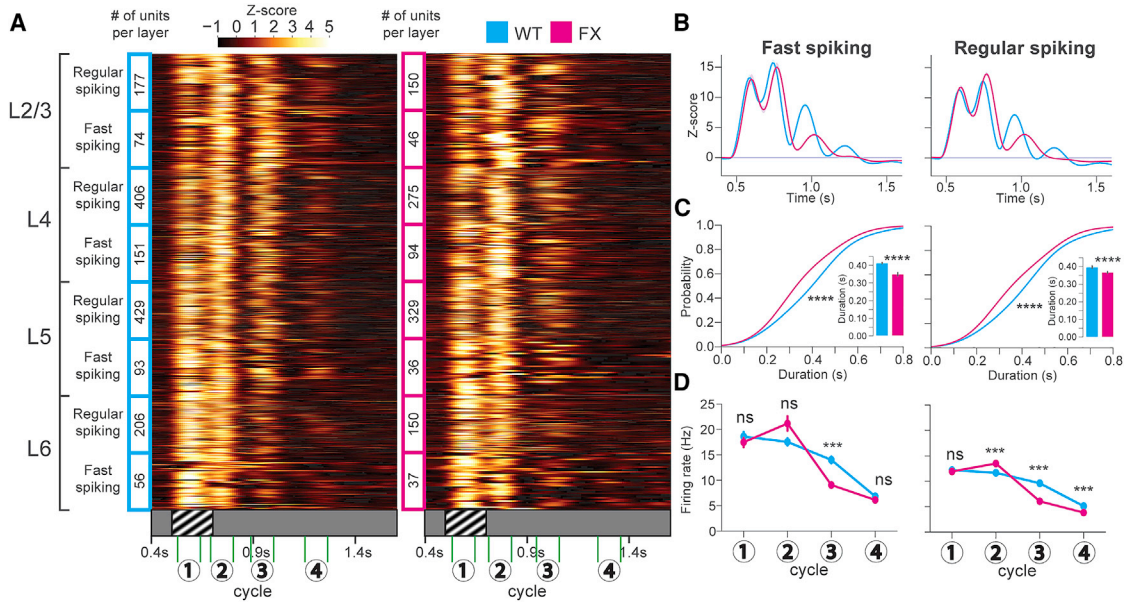

Figure 2. Decreased Duration of Visually Evoked Oscillations in FX Mice

(A) Heatmaps showing the *Z* scored firing rates for oscillatory units from WT (cyan, 31 mice) and FX (magenta, 25 mice) mice after perceptual experience across all layers of V1. The numbers 1–4 indicate the timings of 4 cycles of the oscillation.

(B) Population (across all layers) *Z* score line plots.

(C) Cumulative distributions of oscillation duration. Inset: mean duration bar graphs are shown. FS cells: 2-sample Kolmogorov-Smirnov (KS) test of duration CDFs; WT versus FX duration: D(566) = 0.30; p = 3.81E−11. Welch's t test of mean duration: t(566) = 3.73; p = 2.1E−4 (units after peak detection: WT FS n = 362; FX FS n = 206). RS cells: 2-sample KS test of duration CDFs; WT versus FX duration: D(1,993) = 0.27, p = 1.35E−33. Welch's t test of mean duration: t(1,993) = 6.65; p = 3.77E−11 (units after peak detection: WT RS n = 1,152; FX RS n = 843). Error bars indicate SEM. *p < 0.05; **p < 0.01; ***p < 0.001; ****p < 0.0001.

(D) Mean firing rates at 4 oscillation cycles between WT and FX. LMM analysis for FS cells after perceptual experience: genotype: $F_{1,585}$ = 1.0; p = 0.32. Oscillation no.: $F_{3,1755}$ = 472; p < 1E−4. Genotype/oscillation no. interaction: $F_{3,1755}$ = 27.2; p < 1E−4. LS means test (Bonferroni corrected): cycle(1): estimate: −1.24E−2; t(1,036) = −0.15; p = 1.0. (2): estimate: 0.19; t(1,036) = 2.37; p = 0.07. (3): estimate: −0.41; t(1,036) = −5.08; p < 4E−4. (4): estimate: −4.54E−2; t(1,036) = −0.56; p = 1.0. SE: 8.13E−2. LMM analysis for RS cells after perceptual experience: genotype: $F_{1,2120}$ = 25.5; p < 1E−4. Oscillation no.: $F_{3,6,360}$ = 1,902.23; p = 1E−4. Genotype/oscillation no. interaction: $F_{3,6360}$ = 141.13; p < 1E−4. LS means test (Bonferroni corrected): cycle(1): estimate: −4.05E−2; t(4,333) = −1.34; p = 0.72. (2): estimate: 0.145; t(4,333) = 4.81; p < 4E−4. (3): estimate: −0.41, t(4,333) = −13.7; p < 4E−4. (4): estimate: −0.19; t(4,333) = −6.33; p < 4E−4. SE: 3.02E−2. See also Figures S1–S8 and Table S1.

theta and beta power in WT compared to FX mice (Figures 1G and 1H). These results suggest that, although familiarity to the experienced visual stimulus is encoded in FX mice, it is done so less efficiently. In particular, attenuation in the theta band is consistent with the reported impairments in working memory in FX patients, while attenuation in the beta band is suggestive of impairments in feedback connections that may drive this oscillatory activity (Ethridge et al., 2017; Lee et al., 2005; Lovelace et al., 2018; Munir et al., 2000).

Attenuated Visually Evoked Oscillations in Single Units across Multiple Cortical Layers in FX Mice

To reveal layer- or cell-type-specific differences in oscillatory activity in FX mice, we recorded single-unit activity across all cortical layers of V1 before and after perceptual experience (Figure 2A). Given the prior and recent literature demonstrating reduced inhibition in the cortex of FX mice and other autism models (Antoine et al., 2019; Gibson et al., 2008; Goel et al., 2018), we segregated units into putative RS or FS neurons to understand the relative contributions of each in the expression of perceptual experience-dependent oscillatory activity (Figure S1).

As we discovered previously, the most prominent readout of visual perceptual experience is the transition from a primarily stimulus-locked response to one that is oscillatory and persists for 3–5 (or in rare cases 6) distinct cycles after visual stimulation. To capture this change, we estimated oscillation duration using a peak detection algorithm on the *Z* score time series of each unit (Figure 2B). Before perceptual experience, differences in the mean duration of oscillatory activity were found between WT and FX mice in 3 cell types: RS in L4 and L6 and FS in L4 (Figures S2 and S3). After perceptual experience, we found significant differences in the oscillation duration of 7 cell types: RS and FS neurons in L2/3, L4, and L5 and RS in L6. These decreased durations were evident across the whole population in both male (Figure 2) and homozygous female FX mice (Figures S4A and S4B) as well as in subpopulations of units in different layers (Figures S2 and S3). Specifically, there was less prominent engagement at oscillatory cycles 3 and 4 for FX mice compared to WT (Figures 2B, S2, and S3). This is seen quantitatively as significantly decreased durations (i.e., less persistence) in FX mice compared to the WT at both the population level and in L2/3 and L4 (Figures 2C and S2A–S2D). WT mice also showed higher mean firing rates at the 3rd and 4th cycle in pyramidal cells

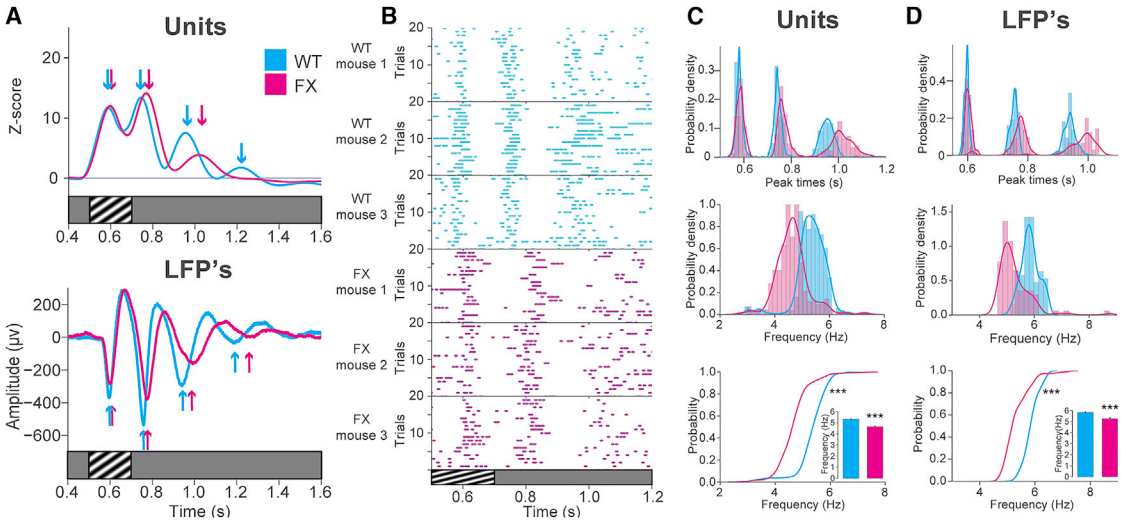

Figure 3. Decreased Frequency of Peak Oscillatory Activity in FX Mice

(A) *Z* scored firing rate for all visually excited units recorded after experience (across all layers) in WT (cyan, 31 mice; n = 1,592 units) and FX (magenta; 25 mice; n = 1,117 units) mice. Arrows indicate the peak response times.

(B) Raster plots of individual units from three WT or FX mice.

(C) Top: distributions of peak times across WT and FX unit populations at 3 oscillation cycles. Middle: distributions of oscillation frequency are shown. Bottom: cumulative distributions of oscillation frequency and mean oscillation frequency (inset) are shown. 2-sample KS test, WT versus FX frequency: D(934) = 0.65; p = 4.36E−73. Welch's t test: t(934) = 16.25; p = 1.87E−47. WT mean frequency = 5.3307 Hz; FX mean frequency = 4.6484 Hz; difference = 0.6823 Hz (units after peak detection: WT: n = 668; FX: n = 268). Error bars indicate SEM. *p < 0.05; **p < 0.01; ***p < 0.001.

(D) Top: distributions of peak times across WT and FX LFPs at 3 oscillation cycles. Middle: distributions of oscillation frequency are shown. Bottom: cumulative distributions of oscillation frequency and mean oscillation frequency (inset) are shown. 2-sample KS test, WT versus FX frequency: D(200) = 0.66; p = 2.15E−20. Welch's t test: t(200) = 8.16; p = 2.22E−13. WT mean frequency = 5.8484 Hz; FX mean frequency = 5.2841 Hz; difference = 0.5643 Hz.

across the population and in L2/3, L4, and L5 as well as at cycle 3 in FS cells in L2/3 and L4 (Figures 2D and S5; Table S1). L5 RS units also displayed significantly shorter mean oscillation durations in FX compared to WT mice, but no significant differences were found in L5 FS or L6 FS or RS cells (Figures S3B–S3D). Presentation of a novel stimulus to a subset of these animals elicited primarily stimulus-locked responses comparable to those seen before perceptual experience (Figure S6). Although the responses were qualitatively not oscillatory, peak detection revealed significant differences in the mean duration between WT and FX in L2/3 RS, L4 FS, and L6 RS cells, likely due to the engagement of cycle 3 for subsets of these units (Figures S6B, S6C, and S6H).

In summary, these results reveal visual experience-dependent oscillations that are less persistent in FX mice, particularly in L2/3 and L4. Consistent with our CSD analysis, these results also demonstrate that the oscillations are more prominent in the single-unit activity of the superficial compared to deep cortical layers.

Decreased Peak Response Frequency of Visually Evoked Oscillations in FX Mice

Across the full population of recorded units as well as VEPs, we noticed delays in the peak response magnitudes in FX compared to WT mice after perceptual experience (Figure 3A). This delay was observed in single-unit activity across all layers and for both RS and FS cells (see Figures S2 and S3 line plots). Raster plots from individual mice in these populations revealed this delay in FX mice robustly across trials, particularly at the later oscillation cycles, where the delay progressively increased (Figure 3B). The distributions of peak times for each cycle across these unit populations also displayed this trend (Figures 3C and 3D, top). We then quantified the mean frequency across these oscillatory cycles between WT and FX mice using the peak responses detected on the *Z* score time series for each unit. Only units with at least 3 distinct oscillatory cycles were considered, such that the period and frequency of peak oscillatory activity in a set of comparable units between WT and FX mice could be determined. Among these units, a significant decrease was seen in the frequency of the peak oscillatory activity in FX compared to WT mice (Figure 3C). There was overlap in the distributions of oscillation frequency for individual units between the two groups, yet the oscillations were lower in frequency in FX mice on average by ~0.68 Hz. Both the distributions of peak times for each cycle and distributions of oscillation frequency from WT and FX female mice trended toward those seen in males, though they did not reach statistical significance in this smaller dataset (Figures S4C and S4D). Quantification of the oscillation frequency for LFP recordings yielded similar results (Figure 3D). These results are consistent with other studies, which have shown that the resonance frequency at which pyramidal cells respond to sinusoidal current injections is decreased by a similar amount in FX mice (Kalmbach et al., 2015; Zhang et al., 2014). We may be seeing the consequences of this resonance frequency decrease but at the scale of neural ensembles evoked by visual stimulation in awake animals.

Decreased Habituation of Visually Evoked Pupil Dynamics in FX Mice

Anxiety, hyperactivity, and hyperarousal are defining characteristics of FX. To determine the arousal state of WT and FX mice, we simultaneously recorded pupil size and locomotion during our recordings. Before the perceptual experience, both WT and FX mice increased their run speed shortly after viewing visual stimuli (Figure S7A). However, no obvious stimulus-evoked running occurred in the post or novel conditions, nor could significant differences be found in the mean running speed or percentage of mobile trials between WT and FX mice (Figures S7A and S7B). Although this observation differs from reports of FX hyperactivity in an open field setting (Dolan et al., 2013; Kramvis et al., 2013), it is consistent with a lack of locomotion differences found in head-fixed FX mice (Goel et al., 2018). On the other hand, pupil diameter is an indirect measurement of locus coeruleus activity and serves as a more robust measure of arousal. Although locomotion is often reported to increase pupil size, the dynamics of that relationship are not necessarily inextricably linked. Within each stimulus condition and within each genotype, the percent increase in pupil size relative to the baseline period was larger for mobile trials, though the response dynamics were different between measurements of pupil size and locomotion (Figure S7D). Consistent with our previous findings, both WT and FX mice displayed a sustained pupillary surprise response when viewing a stimulus for the first time (pre and novel; Kissinger et al., 2018). Although this ''arousal'' response was larger in FX than WT, no significant differences were found during mobile or immobile trials (Figures S7D–S7F). After perceptual experience, this arousal response was attenuated in both WT and FX mice. However, it remained significantly larger in FX compared to WT mice, suggesting decreased experience-dependent habituation to the stimulus. Arousal and locomotion are also known to have profound effects on cortical activity, both decreasing the power of spontaneous low-frequency oscillations in LFPs and exerting a gain modulation to increase firing rates (Niell and Stryker, 2010; Polack et al., 2013; Reimer et al., 2014; Vinck et al., 2015). Consistent with these findings, locomotion decreased the power of all frequency bands during the oscillations and increased firing rates compared to immobile trials in WT and FX mice (Figure S8).

Functional Connectivity Changes across Layers in V1 of FX Mice after Perceptual Experience

As demonstrated above, we observed attenuation of the visually evoked oscillations in multiple layers in FX mice relative to WT controls. Using the subpopulations of units in each layer, we sought to systematically characterize the influence of neural activity between layers to ascertain their relative contributions to visually evoked oscillatory activity in WT and FX mice. There are several methodologies available to infer functional connectivity from extracellularly recorded spikes, which can be based on pairwise rate correlations or the timing of individual spikes relative to each other. Toward this goal, we performed directed information analysis, a non-parametric generalization of Granger causality (Quinn et al., 2011, 2015). Broadly, it estimates how robustly the spike times from one or more parent units are predictive of the spike times of a single recipient unit, allowing one to model more complex dynamics than what could be achieved solely using pairwise correlations. This technique can determine not only the strength of that functional connectivity but also its directionality when the cortical layer of each unit is considered. This analysis cannot assess whether two units are directly connected, and cells just outside of the recorded tissue volume likely exert an influence through common inputs or feedback connections. However, it does provide a snapshot of functional connectivity in V1, much of which should be a result of connections that span the recorded tissue column. Directed information analysis was performed across all cortical layers and neural subtypes in WT and FX mice under each stimulus condition during the post-stimulus oscillatory period (0.7–1.5 s). In some cases, single-parent units were the most predictive of activity in the recipient unit (Figure S9A), although in others, sets of parents were optimal (Figure S9B). In an attempt to minimize the influence of indirect connections, the predictive power of parent-unit activity was considered up to 10 ms prior to the recipient unit (Markov order 10). To capture longer latency direct connections or indirect connections, we performed a concurrent analysis with a Markov order of 30. Connectivity matrices were then constructed for each condition, and the FX connectivity matrices were subtracted from their corresponding WT matrix to detect differences across genotypes (Figure 4). Before perceptual experience, we observed significantly decreased functional connectivity in multiple connections in WT compared to FX, including in the L5 RS → L4 FS, L4 RS → L4 RS, L2/3 RS → L5 FS, and L2/3 FS → L5 RS putative connections (Figure 4A). The results also trended toward stronger connections in FX with a Markov order of 30, though the L5 RS → L2/3 RS connection was strong in WT in this case (Figure S10A). After perceptual experience, we noticed dramatic increases in functional connectivity between all layers in both WT and FX mice relative to the pre-experience condition (Figure 4B). Comparing WT and FX mice, one of the most striking differences observed in the functional connectivity matrices was a decrease in connection strengths from multiple layers onto L4 FS cells in FX mice. Many of these connections were weaker in FX mice, with significant differences occurring at the inferred L2/3 FS→ L4 FS (Markov 10 only), L4 FS → L4 FS, L4 RS → L4 FS, L5 RS → L4 FS, and L6 FS → L4 FS connections (Figures 4B and S10B). There was also significantly stronger connectivity in WT compared to FX from L6 RS → L6 FS (Markov 10; Figure 4B) and L6 FS → L4 FS (Markov 10 and 30), L6 FS → L4 RS (Markov 30), and L6 FS → L2/3 RS (Markov 30) cells, which suggest weaker connections in FX known to be involved in cross-cortical inhibition (Bortone et al., 2014; Olsen et al., 2012). On the other hand, many connections onto L2/3 RS cells were significantly stronger in FX, including the L2/3 RS → L2/3 RS (Markov 10), L4 RS → L2/3 RS (Markov 10), and L5 RS → L2/3 RS (Markov 30) connections (Figures 4B and S10B). Directed information matrices for the novel condition displayed decreased functional connectivity across the layers compared to the post-experience condition but were not identical to the matrices in the pre-experience condition (contrast Figure 4C with Figure 4A). Three functional connections were stronger for FX mice in the novel condition, including the L5 RS → L5 RS, L6 RS → L5 RS (Markov 10 only), and L6 RS → L6 RS connections (Figures 4C and S10C). Together, these results

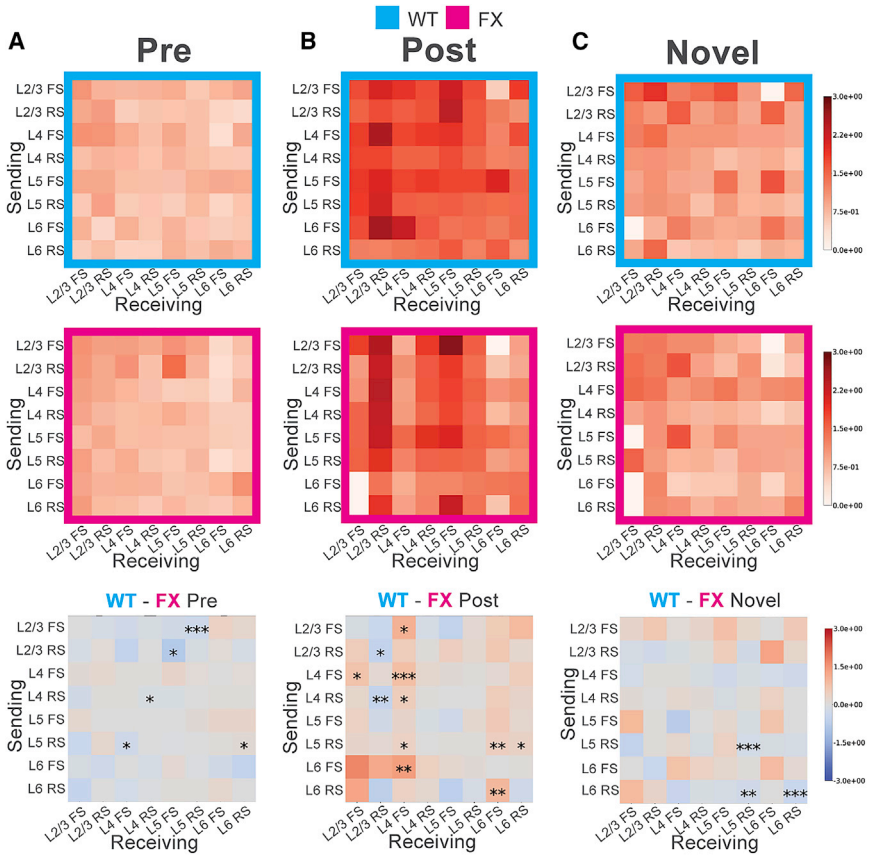

Figure 4. Layer- and Cell-Type-Specific Changes in Functional Connectivity in WT and FX Mice

(A) Functional connectivity (normalized directed information) pre-perceptual experience for WT (cyan) and FX (magenta) mice, where a Markov order of 10 ms was used to compute directed information values. Darker colors indicate stronger (more predictive) connections. The vertical axis indicates cells in different layers sending information, although the horizontal axis indicates cells receiving that information. Bottom: difference between the WT and FX heatmaps is shown. Monte Carlo simulations (10E6 runs) were used to approximate the permutation test for each square in each difference matrix above. Significance levels: *$p < 0.1$; **$p < 0.05$; ***$p < 0.01$.

(B) Functional connectivity post-perceptual experience.

(C) Functional connectivity in response to novel stimuli.

See also Figures S9 and S10.

provide a snapshot of functional connectivity changes after perceptual experience that promote persistent visually evoked oscillations and identify connections in FX mice that might underlie impairments in these oscillations.

Synaptic Connectivity from L5 to L4 RS and FS Neurons following Visual Experience in FX Mice

To directly measure the V1 microcircuit and changes in its plasticity resulting from perceptual experience, we conducted channelrhodopsin-assisted circuit mapping (CRACM) on brain slice preparations (Hooks et al., 2013; Petreanu et al., 2007). Other circuit mapping methods, including paired recordings and glutamate uncaging, have limitations. Paired recordings can measure connectivity between neurons within only 200 μm of each other reliably, as the probability of connectivity decays exponentially with increasing distance, making it unlikely to measure interlaminar connections. Similarly, glutamate uncaging cannot provide the cell type specificity needed to test the connectivity changes observed in our *in vivo* data. Considering that one of the consistent differences in cross-layer functional connectivity in V1 between experienced WT and FX mice occurred at the L5 RS to L4 FS connection, we measured the connectivity of L4 and L5 neurons receiving projections from L5 excitatory neurons in naive and visually experienced animals. We bred homozygote Thy1-ChR2-YFP male mice with heterozygote *Fmr1* KO female mice to perform these experiments. First, we validated that the ChR2 expression levels are not affected by the *Fmr1* KO genotype. There was no significant difference in evoked action potential frequency at a series of light intensity steps between WT and FX age-matched littermates (Figure S11A). To study the effect of the FX genotype on visual experience-induced circuit plasticity, WT and FX littermates with a Thy1-ChR2-YFP background were pseudo-randomly assigned to either naive or experienced groups while the experimenter was blinded to the genotype during data collection. The trained group was subjected to the same habituation and visual perceptual experience as described for the *in vivo* recordings. Acute brain slices were made for CRACM on the day after the end of the perceptual experience.

We performed whole-cell patch clamp recordings of L4 neurons in V1 on acute brain slices from 4 groups of animals: WT naive; FX naive; WT post-experience; and FX post-experience (Figure 5A). To measure local L5 to L4 synaptic strength, we optically stimulated individual cells in a 10 by 10 grid (0.67 mm by 0.67 mm) covering a square area from L2/3 to L5 of V1 using a light patterned illuminator (Figure 5B). For each 10-ms light pulse at each pixel, excitatory post-synaptic currents (EPSCs) were recorded under voltage clamp at −70 mV. All CRACM recordings were conducted with the presence of 10 μM tetrodotoxin (TTX) and 50 μM 4-aminopyridine (4-AP) to block action potentials and thus block multi-synaptic responses to the stimulation. Based on the current-voltage curve measured from step-current injections, there is a bimodal distribution of low and high cell impedance, corresponding to RS excitatory neurons and FS interneurons, respectively (Figures S11B–S11D). For a subpopulation of recorded cells, evoked action potentials were recorded before applying TTX/4-AP. In some recordings, fluorescent dye (Alexa Fluor 594

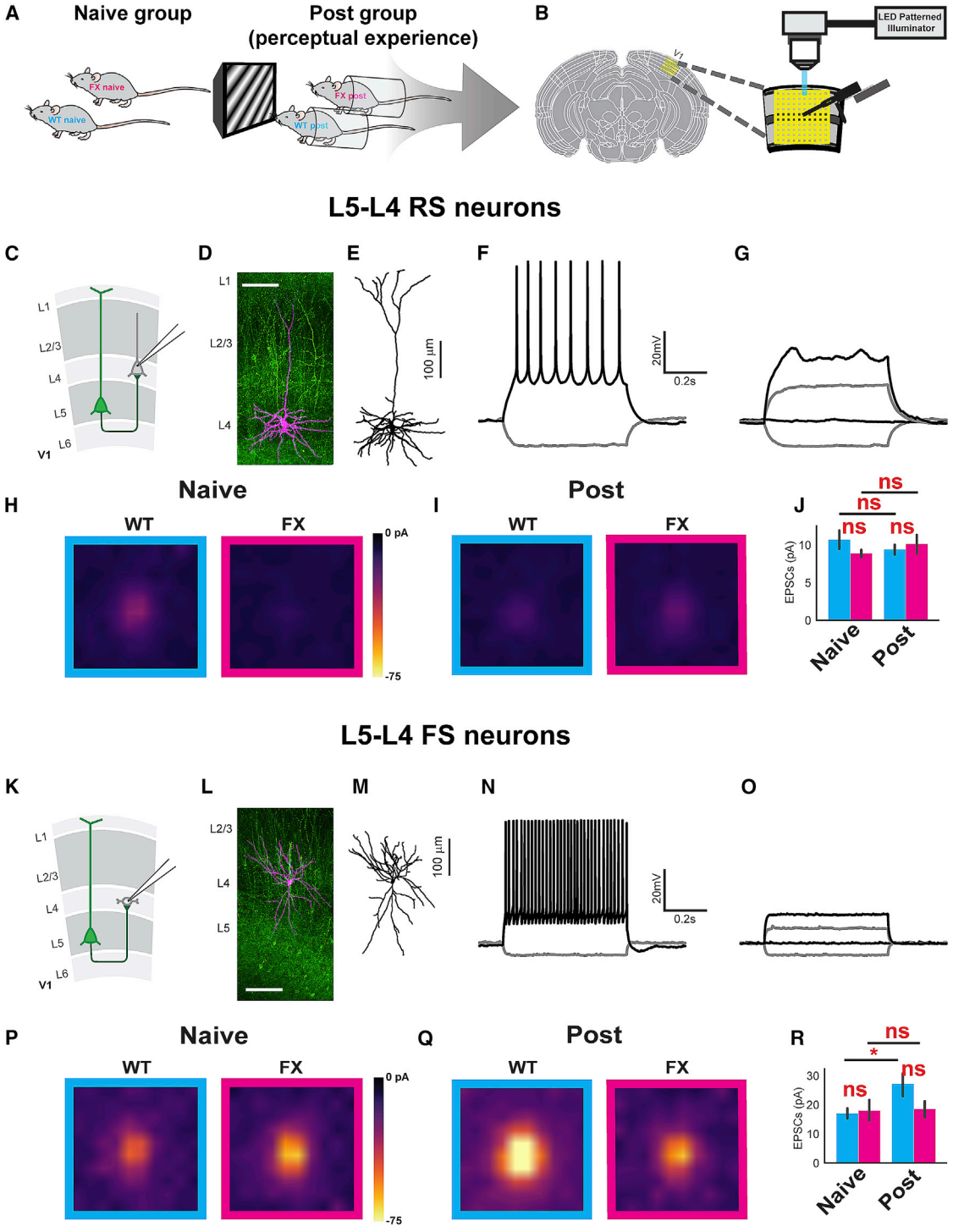

Figure 5. Visual Perceptual Experience Induced Cell-type-Specific Circuit Connectivity Changes from L5 to L4 in V1 of WT and FX Mice

(A) Experimental groups.

(B) Acute visual cortical slices CRACM setup.

(C) Illustration of L5 to L4 RS neuron projections.

(D and L) Example tiled composite confocal image of mapped neurons (magenta) filled with Alexa Fluor 568 Hydrazide (scale bar, 100 μm). The green color indicates ChR2-YFP-positive neurons and processes.

(E and M) Traced neuron from (D) and (L) showing the morphology of specific neuronal types.

(F and N) Step current injection traces showing action potentials corresponding to the neurons shown in (D) and (L).

(legend continued on next page)

Hydrazide) was added to the pipette internal solution to allow for the subsequent reconstruction of cell morphology. There were consistent and expected correlations between impedance and action potential waveform, cell body morphology under differential interference contrast (DIC) optics, and whole-cell morphology following reconstruction that corresponds to cell types (Figures 5C–5G and 5K–5O). We found that there was no significant difference in impedance among RS cells (Figure S11C) and among FS cells (Figure S11D) between the WT and FX groups. Perceptual experience had no effect on cell impedance, as expected (Figure S11E).

To determine any differences in connection strength at the L5-L4 RS connection between WT and FX mice, we first created averaged CRACM maps for each experimental group. Only mild differences were observable in the heatmaps (Figures 5H and 5I). We then averaged the CRACM values for each cell to estimate the global differences in connection strength in accordance with established methodology (Shepherd et al., 2003). These averaged values were then Box-Cox transformed to obtain a normal distribution of EPSCs across cells and compared with a two-way ANOVA and post hoc Tukey test. Neither the main effects of perceptual experience or genotype had a significant effect on the means of the transformed averaged EPSCs (Figure 5J). Next, we examined connectivity changes in the L5-L4 FS connection. The averaged CRACM heatmaps appeared hotter post-visual experience compared to naive for WT, but not FX, mice (Figures 5P and 5Q). This observation was confirmed by quantifying the mean of the $\log_e$ transformed averaged EPSC amplitudes in this connection, which revealed significantly increased synaptic strength after perceptual experience in WT, but not FX, mice relative to the naive state (Figure 5R). However, no significant differences between the mean EPSC values could be found in direct comparisons between WT and FX in either the naive or the post-experience conditions. The potentiation of L5 to L4 FS cells in WT animals after perceptual experience relative to pre and the lack of this change in FX animals largely agree with directed information analysis for this particular connection.

Synaptic Connectivity from L5 to L5 RS and IB Neurons following Visual Experience in FX Mice

We next conducted CRACM measurements on L5 to L5 local connectivity in WT and FX mice, either with or without visual perceptual experience. Putative FS interneurons (identified as described above) were discarded from the analysis due to low cell counts (0–2 cells per group). The remaining putative L5 excitatory neurons were divided into intrinsically bursting (IB) and RS neurons (Figures 6A–6E and 6I–6M) based on input resistance, sag ratio, and the presence/absence of a compensatory current after a depolarizing current step (Figures S11F–S11M). Consistent with the literature, L5 IB cells had lower input resistance and higher sag ratio, as well as a prominent compensatory current after depolarization compared to RS cells (Kasper et al., 1994). Cell types determined by these three parameters were consistent in each of the patched cells and confirmed by cell morphology when available. Because IB cells and RS cells have distinctive projection targets (Kasper et al., 1994) and may contribute to the oscillations in different ways, we analyzed the connectivity of these two groups of cells separately. The averaged CRACM heatmaps for the L5 to L5 RS connection appeared hotter for FX compared to WT in the naive state and for FX in the naive state compared to the post-experience state (Figures 6F and 6G). Although no significant differences could be found in direct comparisons between WT and FX in this connection, a significant depression was observed after perceptual experience in FX mice (Figure 6H). L5 IB cells receiving L5 recurrent projections yielded hotter connectivity heatmaps in both WT and FX compared to the L5-L5 RS connection but did not suggest any difference in connectivity between the experimental groups (Figures 6N and 6O). No significant differences could be found in the mean EPSC strengths of any comparison for this connection (Figure 6P).

DISCUSSION

Attenuation of a Neural Correlate of Visual Familiarity in FX Mice

In this study of a mouse FX model, visual perceptual experience resulted in decreased amplitudes of oscillatory visually evoked potentials in FX mice relative to WT. Considering that LFPs are primarily driven by synaptic activity within the local tissue volume, this attenuation in FX mice may be a result of impaired synaptic plasticity at the connections that drive the oscillation. Decreased theta (4–8 Hz), beta (12–30 Hz), low gamma (30–50 Hz), and high gamma (50–80 Hz) baseline normalized power

(G and O) Step current injection traces with application of TTX/4AP mix corresponding to the neurons shown in (D) and (L).
(H and I) The averaged CRACM maps from L4 RS neurons receiving L5 projections in naive (H) and post (I) WT (cyan) and FX (magenta) animals. WT naive L4 RS: 11 mice, 32 cells. FX naive L4 RS: 11 mice, 39 cells. WT post L4 RS: 10 mice, 33 cells. FX post L4 RS: 10 mice, 39 cells.
(J) Bar graphs showing the averaged EPSC amplitudes for each group ± SEM. Significance is reported from two-way ANOVA followed by Tukey's honest significant difference (HSD) tests to compare the mean Box-Cox transformed EPSCs (two-way ANOVA; no significant interaction was found between genotype and perceptual experience: $F = 0.03$; $p = 0.85$. Main effects after removing the interaction term: genotype: $F = 0.24$; $p = 0.63$. Perceptual experience: $F = 0.22$; $p = 0.64$. Tukey's post hoc: WT naive versus FX naive: $p = 0.66$; WT post versus FX post: $p = 0.83$; WT naive versus WT post: $p = 0.87$; FX naive versus FX post: $p = 0.64$).
(K) L5 to L4 FS neurons projection illustration.
(P and Q) The averaged CRACM map from L4 FS neurons receiving L5 projections in naive (P) and post (Q) WT (cyan) and FX (magenta) animals. WT naive L4 FS: 11 mice, 17 cells. FX naive L4 FS: 11 mice, 11 cells. WT post L4 FS: 10 mice, 15 cells. FX post L4 FS: 10 mice, 7 cells.
(R) Bar graphs showing the averaged EPSC amplitudes for each group ± SEM. Significance is reported from two-way ANOVA followed by Tukey's HSD tests to compare the mean log-transformed EPSCs (two-way ANOVA: no significant interaction was found between the main effects of genotype and perceptual experience: $F = 0.91$; $p = 0.35$. Main effects after removing the interaction term: genotype: $F = 0.85$; $p = 0.36$. Perceptual experience: $F = 5.28$; $p = 0.02$. Tukey's post hoc: WT naive versus FX naive: $p = 0.81$; WT post versus FX post: $p = 0.20$; WT naive versus WT post: $p = 1.79E{-}2$; FX naive versus FX post: $p = 0.63$). See also Figure S11.

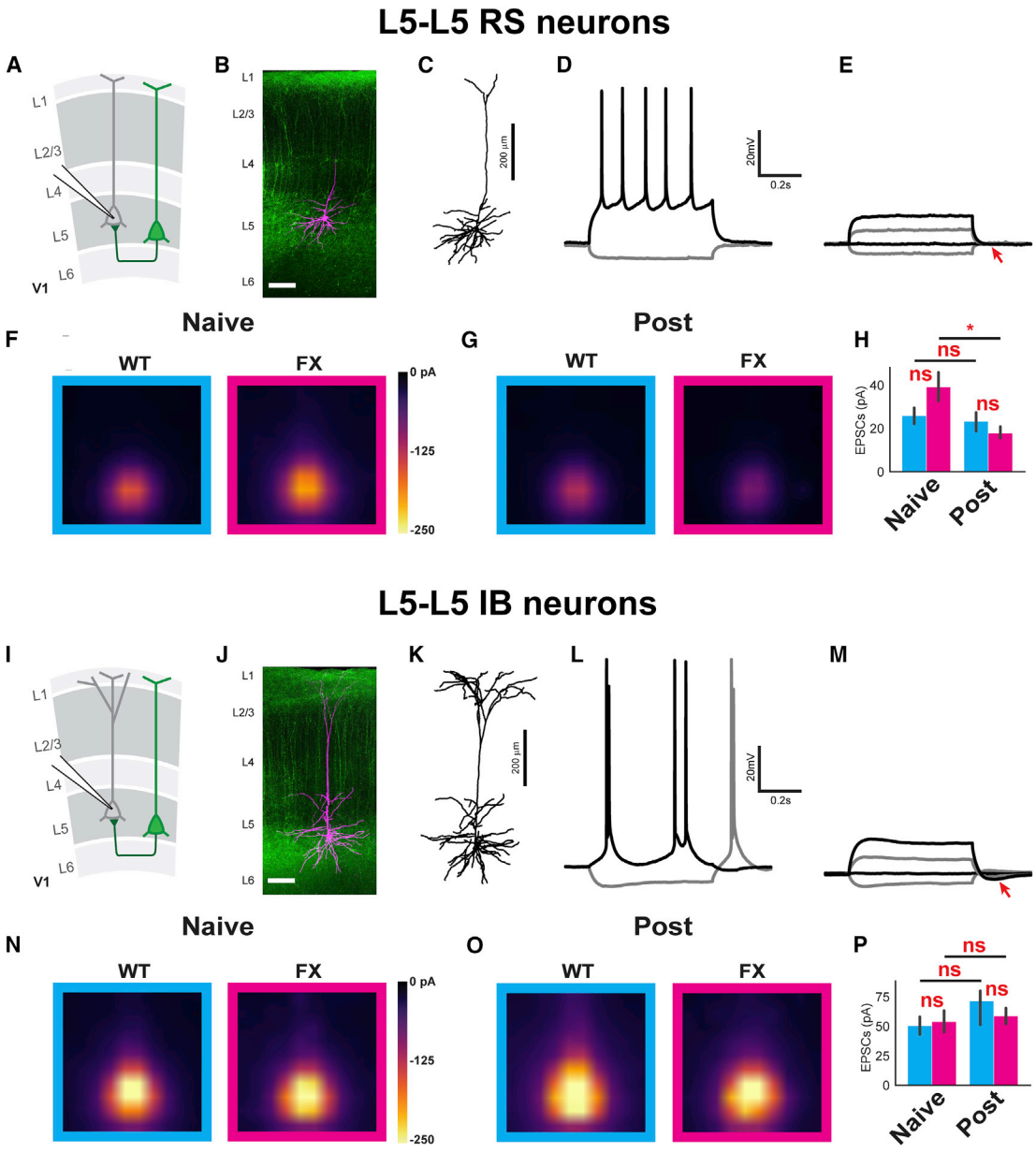

Figure 6. Visual Experience Induced Cell-Type-Specific Local L5 Circuit Connectivity Changes

(A and I) Illustration of L5 to L5 regular spiking pyramidal neuron projections (A) and L5 to L5 intrinsically bursting neuron projections (I).

(B and J) Example tiled composite confocal images of mapped neurons (magenta) filled with Alexa Fluor 568 Hydrazide (scale bars represent 100 μm). The green color indicates ChR2-YFP-positive neurons and processes.

(C and K) Traced neuron from (B) and (J) showing the morphology of specific neuronal types corresponding to (B) and (J).

(D and L) Step current injection traces showing action potentials corresponding to the neurons shown in (B) and (J).

(E and M) Step current injection traces in the presence of TTX/4-AP corresponding to the neurons shown in (B) and (J). The arrow points to the absence/presence of compensatory potential after depolarizing current injection.

(F and G) The averaged CRACM map from L5 RS neurons receiving L5 local projections in naive (F) and post (G) (cyan) and FX (magenta) animals. WT naive L5 RS: 11 mice, 29 cells. FX naive L5 RS: 11 mice, 36 cells. WT post L5 RS: 10 mice, 32 cells. FX post L5 RS: 10 mice, 31 cells.

(H) Bar graphs showing the averaged EPSC amplitudes for each group ± SEM. Significance is reported from two-way ANOVA followed by Tukey's HSD tests to compare the mean Box-Cox transformed EPSCs. Two-way ANOVA, no significant interaction was found between genotype and perceptual experience: $F = 1.24$; $p = 0.26$. Main effects after removing the interaction term: genotype: $F = 0.04$; $p = 0.83$. Perceptual experience: $F = 5.65$; $p = 0.02$. Tukey's post hoc: WT naive versus FX naive: $p = 0.56$; WT post versus FX post: $p = 0.30$; WT naive versus WT post: $p = 0.37$; FX naive versus FX post: $p = 3.46E{-}2$.

(N and O) The averaged CRACM map from L5 intrinsically bursting (IB) neurons receiving L5 local projections in naive (N) and post-WT (O) (cyan) and *Fmr1* KO (magenta) animals. WT naive L5 IB: 11 mice, 19 cells. FX naive L5 IB: 11 mice, 17 cells. WT post L5 IB: 10 mice, 13 cells. FX post L5 IB: 10 mice, 12 cells.

(legend continued on next page)

was also observed in FX compared to WT mice, with alpha power decreased, but not reaching significance. This complex oscillatory profile may point to impairments in a diverse group of recurrent connections in FX mice. The most well-characterized driver of oscillatory activity is the thalamocortical system. Thalamocortical recurrent connectivity is known to drive cortical oscillations over many frequency ranges, the most prominent of which include the alpha (Bollimunta et al., 2011), beta (Bastos et al., 2014), and gamma (McAfee et al., 2018) bands during awake states. Therefore, it is feasible that perceptual experience strengthens thalamocortical recurrent connectivity and that this is impaired in FX mice. Theta, the predominant frequency observed in the oscillations described here, is not a typical thalamocortical generated oscillation in awake states. Rather, thalamocortical theta falls within the lower range of spindle oscillations occurring during sleeping states or absence seizures (Crunelli and Leresche, 2002; Fogerson and Huguenard, 2016). The possibility also remains that the oscillation is generated locally within V1 or is a result of strengthened feedback connections from higher order cortical areas. Different frequency bands have been attributed to the directionality of information flow between visual cortical areas, with theta and gamma associated with feedforward information, although alpha and beta are associated with feedback (Bastos et al., 2015; Michalareas et al., 2016; Richter et al., 2017; van Kerkoerle et al., 2014). Therefore, the differences in oscillatory activity we have observed in V1 of FX may arise from both thalamocortical and interareal influences, though future studies will be necessary to elucidate these possibilities.

The duration of this oscillatory activity was also decreased on average in FX mice compared to WT. Although we still do not fully understand what determines oscillation duration, we can hypothesize that longer durations are representative of better encoding of the visual information. If indeed top-down, local, or thalamocortical feedback connections are important for driving the oscillations, stronger plasticity in these recurrent connections might allow the oscillations to persist longer in the absence of feedforward input. It may also be true that the oscillations are not simply a neural signature of familiarity but represent an active encoding process of that familiarity. As has been demonstrated in the hippocampus, an oscillation can be used to promote cell-type-specific synaptic plasticity (Zarnadze et al., 2016). A common LTP protocol based on an oscillatory stimulus, known as theta burst stimulation, is also known to strengthen synaptic connections (Larson et al., 1986). By analogy, visually evoked oscillations in the cortex may generate a strengthening of synaptic connections that are activated by a familiar stimulus. If the frequency of this oscillatory activity decreases too much, then this visual information may be encoded less efficiently. In turn, the stimulus may resist becoming familiar, despite repeated exposure during the perceptual experience. Although we do not know why the frequency of peak oscillatory activity is decreased in FX mice, we speculate that it may depend on the resonance properties of neurons involved in the oscillatory circuit. Resonance is the frequency at which neurons optimally respond to oscillatory current input and is determined by their passive membrane and channel properties (Hutcheon and Yarom, 2000). Resonance depends on hyperpolarization-activated cyclic nucleotide-gated channel 1 (HCN1), which is expressed extensively in apical dendrites and drives nonselective cation currents after hyperpolarizing input (Narayanan and Johnston, 2007; Zemankovics et al., 2010). L5 pyramidal neurons, driven by optogenetic stimulation of PV+ interneurons in the neocortex, exhibit HCN1-dependent theta resonance (Stark et al., 2013). Decreased resonance frequency has been observed in the primary somatosensory cortex (S1) and the prefrontal cortex of FX mice compared to WT controls (Kalmbach et al., 2015; Zhang et al., 2014). The intrinsic properties of the HCN1 channels in S1 appear normal in FX mice, but their expression levels are significantly reduced in FX mice, which may account for the resonance frequency shift (Zhang et al., 2014). Our results reveal both attenuated oscillatory power together with an altered temporal profile, though whether and how these results are related to each other remain unclear.

Impaired Connectivity in V1 after Perceptual Experience in FX Mice

Directed information, a non-parametric measure of Granger causality, can be used to estimate the functional connectivity between different groups of neurons (Quinn et al., 2011). Performing this analysis between all cortical layers and between RS and FS cells has allowed us to ascertain the cortical wide changes in functional connectivity induced by perceptual experience, as well as the key differences in that connectivity between WT and FX mice. The largest number of significant differences between WT and FX occurred at functional connections from multiple layers and cell types onto L4 FS cells. Previous work has demonstrated impaired excitatory drive onto inhibitory cells in L4 of somatosensory cortex in FX mice (Gibson et al., 2008). Reduced visually evoked activity in PV cells has also been observed in FX mice, and increasing that activity with designer receptors exclusively activated by designer drugs (DREADDs) has been shown to increase performance on a visual discrimination task (Goel et al., 2018). This decreased inhibition in FX mice has long been thought to underlie the cortical hyperexcitability seen in FX, though recent work has suggested that this E/I imbalance is representative of a compensatory mechanism to preserve the peak depolarization of neurons rather than increase it (Antoine et al., 2019).

(P) Bar graphs showing the averaged EPSC amplitudes for each group ± SEM. Significance is reported from two-way ANOVA followed by Tukey's HSD tests to compare the mean raw EPSCs (two-way ANOVA, no significant interaction was found between genotype and perceptual experience: $F = 0.6885$; $p = 0.41$. Main effects after removing the interaction term: genotype: $F = 0.11$; $p = 0.74$. Perceptual experience: $F = 1.88$; $p = 0.18$. Tukey's post hoc: WT naive versus FX naive: $p = 0.77$ WT post versus FX post: $p = 0.45$; WT naive versus WT post: $p = 0.16$; FX naive versus FX post: $p = 0.71$).
See also Figure S11.

Another significant difference in functional connectivity was observed from L6 FS cells onto L4 FS cells. Excitatory cells in L6 have been shown to inhibit the activity of all other layers of V1, suppressing them primarily via intracortical connections but also through indirect suppression of the dorsolateral geniculate nucleus (dLGN) via the thalamic reticular nucleus (Olsen et al., 2012). Interestingly, the intracortical inhibition driven by these L6 excitatory cells occurs at least in part due to their activation of FS inhibitory cells in L6 that send axonal arborizations across all other layers (Bortone et al., 2014). Consistent with these ideas, we also observed significantly stronger functional connectivity from L6 RS cells onto these L6 FS cells in WT compared to FX. These differences were not observed in the pre-experience or novel conditions.

Although L4 interneurons are well known for their role in feedforward inhibition of thalamocortical input, less is understood about the role of intracortical feedback connections onto these cells. Within the context of our study, we can only speculate as to why the L5 RS to L4 FS connection may be important for the propagation of visually evoked oscillatory activity. A computational model offers one possibility, where an IB pyramidal cell can form connections onto a FS interneuron, which then connects to a RS cell that closes the loop by connecting back onto the IB cell and forming an oscillator (Visser and Van Gils, 2014). One feature of this model is the generation of bursts of action potentials within the recurrently connected IB cells, which is dependent on the I_h current. Another feature of the model is the feedback connection between the L5 IB cells and the FS interneurons. The weakening of this connection leads to the abolishment of the theta oscillation within the network, consistent with our *in vivo* functional connectivity and *in vitro* synaptic connectivity measurements.

FMRP is a transcriptional master switch that is upstream of many synaptic-plasticity-related proteins (Niere et al., 2012; Sidorov et al., 2013). The absence of FMRP leads to exaggerated mGluR-dependent LTD in the hippocampus and cortex and an elevated threshold for LTP (Huber et al., 2002; Yun and Trommer, 2011). Here, we systematically measured synaptic connections within the V1 microcircuit with and without perceptual experience in WT and FX mice. We observed a general shift toward depression (smaller magnitude of potentiation and/or larger magnitude of depression) in FX compared to WT mice after perceptual experience. This finding is consistent with the previous observations of enhanced LTD and decreased LTP in FX mice (Huber et al., 2002; Lauterborn et al., 2007; Yun and Trommer, 2011).

Measuring visual cortical circuit connectivity before and after visual experience has allowed us to identify the synaptic connections that changed after perceptual experience and verify connectivity differences identified in the *in vivo* spiking data. We have identified strengthening of the intracortical connections from L5 pyramidal cells onto FS inhibitory interneurons in L4 after perceptual experience in WT, but not FX, mice. As described previously, computational modeling suggests that the strengthening of excitatory to inhibitory connections may be critical for the generation and propagation of low-frequency oscillations in a cortical circuit (Visser and Van Gils, 2014). The lack of strengthening of the L5 RS to L4 FS connection in FX mice may partially explain the weaker and shorter oscillations observed after visual experience in these mice. Interestingly, following visual experience, synaptic strengths in V1 are not uniformly strengthened to the same magnitude. Some remained stable although others slightly weakened (Figures 5 and 6). The differential plasticity at different synapses of the circuit may be important for achieving this oscillatory behavior.

Given its expression in dendrites, the cell body, and axons and its role as a translational regulator, loss of FMRP is expected to have diverse consequences on neural activity (Christie et al., 2009; Darnell et al., 2011). Altered expression of proteins involved in synaptic plasticity may lead to an altered profile of synaptic weights within the microcircuit and, consequently, weaker oscillations, although the frequency shift may be mediated by reduced HCN1 expression and impaired dendritic I_h function. Our work suggests that the identification of impairments in experience-dependent neural activity at both large scales across cortical layers and in the local microcircuitry may be critical for understanding the pathophysiology of FX in sensory systems. Furthermore, this work has strengthened our understanding of the circuit mechanisms driving the visually evoked oscillations themselves, allowing us to better use this visual perceptual experience paradigm to study models of intellectual disability or diseases impacting visual learning and memory.

STAR★METHODS

Detailed methods are provided in the online version of this paper and include the following:

- KEY RESOURCES TABLE
- LEAD CONTACT AND MATERIALS AVAILABILITY
- EXPERIMENTAL MODEL AND SUBJECT DETAILS
- METHOD DETAILS
  - Surgical Procedures
  - Visual Stimulation
  - Data Acquisition and Python Packages
  - LFP analysis
  - Spike detection and sorting
  - Single unit analysis
  - Directed Information Analysis
  - Cross Correlation Analysis of Unit Pairs
  - Pupillometry and Locomotion Analysis
  - *Ex vivo* acute cortical slice preparation
  - Whole-cell patch clamp recording
  - Channelrhodopsin-assisted Circuit Mapping (CRACM)
  - Perfusions, Histology and Imaging
- QUANTIFICATION AND STATISTICAL ANALYSIS
- DATA AND CODE AVAILABILITY

SUPPLEMENTAL INFORMATION

Supplemental Information can be found online at https://doi.org/10.1016/j.celrep.2020.03.050.

ACKNOWLEDGMENTS

We are grateful for the financial support from the National Institutes of Health (NIH) grant R01 MH116500. We thank Dr. Sotiris Masmanidis for the provided silicon probes. We thank Purdue Statistical Consulting Service for the advice on statistical analysis.

AUTHOR CONTRIBUTIONS

S.T.K., Q.W., and A.A.C. designed experiments. S.T.K., Q.W., and A.K.A. performed experiments. S.T.K., Q.W., C.J.Q., A.P., and A.A.C. analyzed data. S.T.K., Q.W., C.J.Q., and A.A.C. wrote the manuscript.

DECLARATION OF INTERESTS

The authors declare no competing interests.

Received: June 10, 2019
Revised: January 30, 2020
Accepted: March 16, 2020
Published: April 7, 2020

REFERENCES

Aizenman, C.D., Kirkwood, A., and Bear, M.F. (1996). A current source density analysis of evoked responses in slices of adult rat visual cortex: implications for the regulation of long-term potentiation. Cereb. Cortex *6*, 751–758.

Antoine, M.W., Langberg, T., Schnepel, P., and Feldman, D.E. (2019). Increased excitation-inhibition ratio stabilizes synapse and circuit excitability in four autism mouse models. Neuron *101*, 648–661.e4.

Avants, B.W., Murphy, D.B., Dapello, J.A., and Robinson, J.T. (2015). NeuroPG: open source software for optical pattern generation and data acquisition. Front. Neuroeng. *8*, 1.

Bastos, A.M., Briggs, F., Alitto, H.J., Mangun, G.R., and Usrey, W.M. (2014). Simultaneous recordings from the primary visual cortex and lateral geniculate nucleus reveal rhythmic interactions and a cortical source for γ-band oscillations. J. Neurosci. *34*, 7639–7644.

Bastos, A.M., Vezoli, J., Bosman, C.A., Schoffelen, J.M., Oostenveld, R., Dowdall, J.R., De Weerd, P., Kennedy, H., and Fries, P. (2015). Visual areas exert feedforward and feedback influences through distinct frequency channels. Neuron *85*, 390–401.

Benjamini, Y., and Hochberg, Y. (1995). Controlling the false discovery rate: a practical and powerful approach to multiple testing. J. R. Stat. Soc. B *57*, 289–300.

Berry-Kravis, E. (2014). Mechanism-based treatments in neurodevelopmental disorders: fragile X syndrome. Pediatr. Neurol. *50*, 297–302.

Bhattacharya, A., Kaphzan, H., Alvarez-Dieppa, A.C., Murphy, J.P., Pierre, P., and Klann, E. (2012). Genetic removal of p70 S6 kinase 1 corrects molecular, synaptic, and behavioral phenotypes in fragile X syndrome mice. Neuron *76*, 325–337.

Bollimunta, A., Mo, J., Schroeder, C.E., and Ding, M. (2011). Neuronal mechanisms and attentional modulation of corticothalamic α oscillations. J. Neurosci. *31*, 4935–4943.

Bortone, D.S., Olsen, S.R., and Scanziani, M. (2014). Translaminar inhibitory cells recruited by layer 6 corticothalamic neurons suppress visual cortex. Neuron *82*, 474–485.

Christie, S.B., Akins, M.R., Schwob, J.E., and Fallon, J.R. (2009). The FXG: a presynaptic fragile X granule expressed in a subset of developing brain circuits. J. Neurosci. *29*, 1514–1524.

Cohen, M.X. (2015). Analyzing Neural Time Series Data: Theory and Practice (MIT).

Crunelli, V., and Leresche, N. (2002). Childhood absence epilepsy: genes, channels, neurons and networks. Nat. Rev. Neurosci. *3*, 371–382.

Darnell, J.C., Van Driesche, S.J., Zhang, C., Hung, K.Y., Mele, A., Fraser, C.E., Stone, E.F., Chen, C., Fak, J.J., Chi, S.W., et al. (2011). FMRP stalls ribosomal translocation on mRNAs linked to synaptic function and autism. Cell *146*, 247–261.

Dolan, B.M., Duron, S.G., Campbell, D.A., Vollrath, B., Shankaranarayana Rao, B.S., Ko, H.Y., Lin, G.G., Govindarajan, A., Choi, S.Y., and Tonegawa, S. (2013). Rescue of fragile X syndrome phenotypes in Fmr1 KO mice by the small-molecule PAK inhibitor FRAX486. Proc. Natl. Acad. Sci. USA *110*, 5671–5676.

Dupret, D., O'Neill, J., and Csicsvari, J. (2013). Dynamic reconfiguration of hippocampal interneuron circuits during spatial learning. Neuron *78*, 166–180.

Ethridge, L.E., White, S.P., Mosconi, M.W., Wang, J., Pedapati, E.V., Erickson, C.A., Byerly, M.J., and Sweeney, J.A. (2017). Neural synchronization deficits linked to cortical hyper-excitability and auditory hypersensitivity in fragile X syndrome. Mol. Autism *8*, 22.

Farzin, F., Whitney, D., Hagerman, R.J., and Rivera, S.M. (2008). Contrast detection in infants with fragile X syndrome. Vision Res. *48*, 1471–1478.

Farzin, F., Rivera, S.M., and Whitney, D. (2011). Resolution of spatial and temporal visual attention in infants with fragile X syndrome. Brain *134*, 3355–3368.

Fogerson, P.M., and Huguenard, J.R. (2016). Tapping the brakes: cellular and synaptic mechanisms that regulate thalamic oscillations. Neuron *92*, 687–704.

Freund, L.S., and Reiss, A.L. (1991). Cognitive profiles associated with the fra(X) syndrome in males and females. Am. J. Med. Genet. *38*, 542–547.

Gallagher, A., and Hallahan, B. (2012). Fragile X-associated disorders: a clinical overview. J. Neurol. *259*, 401–413.

Gallego, P.K., Burris, J.L., and Rivera, S.M. (2014). Visual motion processing deficits in infants with the fragile X premutation. J. Neurodev. Disord. *6*, 29.

Gibson, J.R., Bartley, A.F., Hays, S.A., and Huber, K.M. (2008). Imbalance of neocortical excitation and inhibition and altered UP states reflect network hyperexcitability in the mouse model of fragile X syndrome. J. Neurophysiol. *100*, 2615–2626.

Goel, A., Cantu, D.A., Guilfoyle, J., Chaudhari, G.R., Newadkar, A., Todisco, B., de Alba, D., Kourdougli, N., Schmitt, L.M., Pedapati, E., et al. (2018). Impaired perceptual learning in a mouse model of Fragile X syndrome is mediated by parvalbumin neuron dysfunction and is reversible. Nat. Neurosci. *21*, 1404–1411.

Gonçalves, J.T., Anstey, J.E., Golshani, P., and Portera-Cailliau, C. (2013). Circuit level defects in the developing neocortex of Fragile X mice. Nat. Neurosci. *16*, 903–909.

Granger, C.W.J. (1969). Investigating causal relations by econometric models and cross-spectral methods. Econometrica *37*, 424–438.

Grünwald, P.D. (2007). The Minimum Description Length Principle (MIT).

Hall, S.S., Lightbody, A.A., and Reiss, A.L. (2008). Compulsive, self-injurious, and autistic behavior in children and adolescents with fragile X syndrome. Am. J. Ment. Retard. *113*, 44–53.

Harris, S.W., Hessl, D., Goodlin-Jones, B., Ferranti, J., Bacalman, S., Barbato, I., Tassone, F., Hagerman, P.J., Herman, H., and Hagerman, R.J. (2008). Autism profiles of males with fragile X syndrome. Am. J. Ment. Retard. *113*, 427–438.

Hays, S.A., Huber, K.M., and Gibson, J.R. (2011). Altered neocortical rhythmic activity states in Fmr1 KO mice are due to enhanced mGluR5 signaling and involve changes in excitatory circuitry. J. Neurosci. *31*, 14223–14234.

Hooks, B.M., Mao, T., Gutnisky, D.A., Yamawaki, N., Svoboda, K., and Shepherd, G.M. (2013). Organization of cortical and thalamic input to pyramidal neurons in mouse motor cortex. J. Neurosci. *33*, 748–760.

Hou, L., Antion, M.D., Hu, D., Spencer, C.M., Paylor, R., and Klann, E. (2006). Dynamic translational and proteasomal regulation of fragile X mental retardation protein controls mGluR-dependent long-term depression. Neuron *51*, 441–454.

Huber, K.M., Gallagher, S.M., Warren, S.T., and Bear, M.F. (2002). Altered synaptic plasticity in a mouse model of fragile X mental retardation. Proc. Natl. Acad. Sci. USA *99*, 7746–7750.

Hutcheon, B., and Yarom, Y. (2000). Resonance, oscillation and the intrinsic frequency preferences of neurons. Trends Neurosci. *23*, 216–222.

Kalmbach, B.E., Johnston, D., and Brager, D.H. (2015). Cell-type specific channelopathies in the prefrontal cortex of the fmr1-/y mouse model of Fragile X syndrome. eNeuro *2*, ENEURO.0114-15.2015.

Kasper, E.M., Larkman, A.U., Lübke, J., and Blakemore, C. (1994). Pyramidal neurons in layer 5 of the rat visual cortex. I. Correlation among cell morphology, intrinsic electrophysiological properties, and axon targets. J. Comp. Neurol. *339*, 459–474.

Kissinger, S.T., Pak, A., Tang, Y., Masmanidis, S.C., and Chubykin, A.A. (2018). Oscillatory encoding of visual stimulus familiarity. J. Neurosci. *38*, 6223–6240.

Koga, K., Liu, M.G., Qiu, S., Song, Q., O'Den, G., Chen, T., and Zhuo, M. (2015). Impaired presynaptic long-term potentiation in the anterior cingulate cortex of Fmr1 knock-out mice. J. Neurosci. *35*, 2033–2043.

Kramvis, I., Mansvelder, H.D., Loos, M., and Meredith, R. (2013). Hyperactivity, perseveration and increased responding during attentional rule acquisition in the Fragile X mouse model. Front. Behav. Neurosci. *7*, 172.

Larson, J., Wong, D., and Lynch, G. (1986). Patterned stimulation at the theta frequency is optimal for the induction of hippocampal long-term potentiation. Brain Res. *368*, 347–350.

Larson, J., Jessen, R.E., Kim, D., Fine, A.K., and du Hoffmann, J. (2005). Age-dependent and selective impairment of long-term potentiation in the anterior piriform cortex of mice lacking the fragile X mental retardation protein. J. Neurosci. *25*, 9460–9469.

Lauterborn, J.C., Rex, C.S., Kramár, E., Chen, L.Y., Pandyarajan, V., Lynch, G., and Gall, C.M. (2007). Brain-derived neurotrophic factor rescues synaptic plasticity in a mouse model of fragile X syndrome. J. Neurosci. *27*, 10685–10694.

Lee, H., Simpson, G.V., Logothetis, N.K., and Rainer, G. (2005). Phase locking of single neuron activity to theta oscillations during working memory in monkey extrastriate visual cortex. Neuron *45*, 147–156.

Łeski, S., Wójcik, D.K., Tereszczuk, J., Swiejkowski, D.A., Kublik, E., and Wróbel, A. (2007). Inverse current-source density method in 3D: reconstruction fidelity, boundary effects, and influence of distant sources. Neuroinformatics *5*, 207–222.

Lovelace, J.W., Ethell, I.M., Binder, D.K., and Razak, K.A. (2018). Translation-relevant EEG phenotypes in a mouse model of Fragile X Syndrome. Neurobiol. Dis. *115*, 39–48.

Marko, H. (1973). The bidirectional communication theory - a generalization of information theory. IEEE Trans. Commun. *21*, 1345–1351.

Martin, H.G.S., Lassalle, O., Brown, J.T., and Manzoni, O.J. (2016). Age-dependent long-term potentiation deficits in the prefrontal cortex of the Fmr1 knockout mouse model of Fragile X syndrome. Cereb. Cortex *26*, 2084–2092.

McAfee, S.S., Liu, Y., Dhamala, M., and Heck, D.H. (2018). Thalamocortical communication in the awake mouse visual system involves phase synchronization and rhythmic spike synchrony at high gamma frequencies. Front. Neurosci. *12*, 837.

Michalareas, G., Vezoli, J., van Pelt, S., Schoffelen, J.M., Kennedy, H., and Fries, P. (2016). Alpha-beta and gamma rhythms subserve feedback and feedforward influences among human visual cortical areas. Neuron *89*, 384–397.

Mitzdorf, U. (1985). Current source-density method and application in cat cerebral cortex: investigation of evoked potentials and EEG phenomena. Physiol. Rev. *65*, 37–100.

Munir, F., Cornish, K.M., and Wilding, J. (2000). Nature of the working memory deficit in fragile-X syndrome. Brain Cogn. *44*, 387–401.

Narayanan, R., and Johnston, D. (2007). Long-term potentiation in rat hippocampal neurons is accompanied by spatially widespread changes in intrinsic oscillatory dynamics and excitability. Neuron *56*, 1061–1075.

Niell, C.M., and Stryker, M.P. (2010). Modulation of visual responses by behavioral state in mouse visual cortex. Neuron *65*, 472–479.

Niere, F., Wilkerson, J.R., and Huber, K.M. (2012). Evidence for a fragile X mental retardation protein-mediated translational switch in metabotropic glutamate receptor-triggered Arc translation and long-term depression. J. Neurosci. *32*, 5924–5936.

Nosyreva, E.D., and Huber, K.M. (2006). Metabotropic receptor-dependent long-term depression persists in the absence of protein synthesis in the mouse model of fragile X syndrome. J. Neurophysiol. *95*, 3291–3295.

Olsen, S.R., Bortone, D.S., Adesnik, H., and Scanziani, M. (2012). Gain control by layer six in cortical circuits of vision. Nature *483*, 47–52.

Pachitariu, M., Steinmetz, N., Kadir, S., Carandini, M., and Kenneth, D.H. (2016). Kilosort: realtime spike-sorting for extracellular electrophysiology with hundreds of channels. bioRxiv. https://doi.org/10.1101/061481.

Petreanu, L., Huber, D., Sobczyk, A., and Svoboda, K. (2007). Channelrhodopsin-2-assisted circuit mapping of long-range callosal projections. Nat. Neurosci. *10*, 663–668.

Pettersen, K.H., Devor, A., Ulbert, I., Dale, A.M., and Einevoll, G.T. (2006). Current-source density estimation based on inversion of electrostatic forward solution: effects of finite extent of neuronal activity and conductivity discontinuities. J. Neurosci. Methods *154*, 116–133.

Polack, P.O., Friedman, J., and Golshani, P. (2013). Cellular mechanisms of brain state-dependent gain modulation in visual cortex. Nat. Neurosci. *16*, 1331–1339.

Portera-Cailliau, C. (2012). Which comes first in fragile X syndrome, dendritic spine dysgenesis or defects in circuit plasticity? Neuroscientist *18*, 28–44.

Quinn, C.J., Coleman, T.P., Kiyavash, N., and Hatsopoulos, N.G. (2011). Estimating the directed information to infer causal relationships in ensemble neural spike train recordings. J. Comput. Neurosci. *30*, 17–44.

Quinn, C.J., Kiyavash, N., and Coleman, T.P. (2015). Directed information graphs. IEEE Trans. Inf. Theory *61*, 6887–6909.

Reimer, J., Froudarakis, E., Cadwell, C.R., Yatsenko, D., Denfield, G.H., and Tolias, A.S. (2014). Pupil fluctuations track fast switching of cortical states during quiet wakefulness. Neuron *84*, 355–362.

Richter, C.G., Thompson, W.H., Bosman, C.A., and Fries, P. (2017). Top-down beta enhances bottom-up gamma. J. Neurosci. *37*, 6698–6711.

Rossant, C., Kadir, S.N., Goodman, D.F.M., Schulman, J., Hunter, M.L.D., Saleem, A.B., Grosmark, A., Belluscio, M., Denfield, G.H., Ecker, A.S., et al. (2016). Spike sorting for large, dense electrode arrays. Nat. Neurosci. *19*, 634–641.

Schreiber, T. (2000). Measuring information transfer. Phys. Rev. Lett. *85*, 461–464.

Shepherd, G.M., Pologruto, T.A., and Svoboda, K. (2003). Circuit analysis of experience-dependent plasticity in the developing rat barrel cortex. Neuron *38*, 277–289.

Shobe, J.L., Claar, L.D., Parhami, S., Bakhurin, K.I., and Masmanidis, S.C. (2015). Brain activity mapping at multiple scales with silicon microprobes containing 1,024 electrodes. J. Neurophysiol. *114*, 2043–2052.

Sidorov, M.S., Auerbach, B.D., and Bear, M.F. (2013). Fragile X mental retardation protein and synaptic plasticity. Mol. Brain *6*, 15.

Stark, E., Eichler, R., Roux, L., Fujisawa, S., Rotstein, H.G., and Buzsáki, G. (2013). Inhibition-induced theta resonance in cortical circuits. Neuron *80*, 1263–1276.

van Kerkoerle, T., Self, M.W., Dagnino, B., Gariel-Mathis, M.A., Poort, J., van der Togt, C., and Roelfsema, P.R. (2014). Alpha and gamma oscillations characterize feedback and feedforward processing in monkey visual cortex. Proc. Natl. Acad. Sci. USA *111*, 14332–14341.

Vinck, M., Batista-Brito, R., Knoblich, U., and Cardin, J.A. (2015). Arousal and locomotion make distinct contributions to cortical activity patterns and visual encoding. Neuron *86*, 740–754.

Visser, S., and Van Gils, S.A. (2014). Lumping Izhikevich neurons. EPJ Nonlinear Biomed. Phys. *2*, 6.

Wu, Q., and Chubykin, A.A. (2017). Application of automated image-guided patch clamp for the study of neurons in brain slices. J. Vis. Exp., 56010.

Wu, Q., Kolb, I., Callahan, B.M., Su, Z., Stoy, W., Kodandaramaiah, S.B., Neve, R., Zeng, H., Boyden, E.S., Forest, C.R., and Chubykin, A.A. (2016). Integration of autopatching with automated pipette and cell detection in vitro. J. Neurophysiol. *116*, 1564–1578.

Yun, S.H., and Trommer, B.L. (2011). Fragile X mice: reduced long-term potentiation and N-Methyl-D-Aspartate receptor-mediated neurotransmission in dentate gyrus. J. Neurosci. Res. *89*, 176–182.

Zarnadze, S., Bäuerle, P., Santos-Torres, J., Böhm, C., Schmitz, D., Geiger, J.R., Dugladze, T., and Gloveli, T. (2016). Cell-specific synaptic plasticity induced by network oscillations. eLife *5*, e14912.

Zemankovics, R., Káli, S., Paulsen, O., Freund, T.F., and Hájos, N. (2010). Differences in subthreshold resonance of hippocampal pyramidal cells and interneurons: the role of h-current and passive membrane characteristics. J. Physiol. *588*, 2109–2132.

Zhang, Y., Bonnan, A., Bony, G., Ferezou, I., Pietropaolo, S., Ginger, M., Sans, N., Rossier, J., Oostra, B., LeMasson, G., and Frick, A. (2014). Dendritic channelopathies contribute to neocortical and sensory hyperexcitability in Fmr1(-/y) mice. Nat. Neurosci. *17*, 1701–1709.

STAR★METHODS

KEY RESOURCES TABLE

REAGENT or RESOURCE	SOURCE	IDENTIFIER
Chemicals, Peptides, and Recombinant Proteins		
Monosodium Phosphate	Santa Cruz	sc-202342
Sodium Bicarbonate	DOT scientific, Inc	DSS22060
Dextrose	DOT scientific, Inc	7203B
Sodium Chloride	DOT scientific, Inc	DSS23020
Calcium Chloride	DOT scientific, Inc	DSC20010
Magnesium Chloride	DOT scientific, Inc	DSM24000
Potassium Chloride	DOT scientific, Inc	DSP41000
Alexa Fluor 594 Hydrazide	ThermoFisher Scientific	A10438
Phosphocreatine	Sigma-Aldrich	P7936
GTP	Sigma-Aldrich	G8877
ATP	Sigma-Aldrich	A9187
Ascorbic Acid	DOT scientific, Inc	DSA50040
HEPES	Sigma-Aldrich	H3375
Experimental Models: Organisms/Strains		
C57BL/6	The Jackson Laboratory	C57BL/6
Fmr1 KO	The Jackson Laboratory	*Fmr1* KO
Software and Algorithms		
Python	Python	Version 2.7
Anaconda Distribution	Anaconda Inc.	Anaconda for Python 2.7
MATLAB	Mathworks	MATLAB
SAS	SAS Institute	SAS
Other		
C&B-Metabond® Quick! Cement System	Parkell	S380
ZIP Kicker CA accelerator	ZAP Glue	#PT-27
LOCTITE super glue ultragel control	LOCTITE	SKU #688626 (Home Depot)
Animal Temperature Controller	World Precision Instruments (WPI)	ATC-2000
Motorized Stereotax	Neurostar	Single robot stereotax
Isoflurane Vaporizer	Parkland Scientific	V3000PK
Micromanipulator	Scientifica	PatchStar Micromanipulator with PatchPad
Stereo Microscope	AmScope	SM-4TZ-144A
Aluminum Breadboard 12” x 18” x 1/2,” 1/4”-20 Taps	Thorlabs	MB1218
Miniature V-Clamp, 0.42” Long, M4 Tapped Hole	Thorlabs	VH1/M
Ø1.25” Studded Pedestal Base Adaptor, 1/4”-20 Thread	Thorlabs	BE1
Short Clamping Fork, 1.24” Counterbored Slot, 1/4”-20 Captive Screw	Thorlabs	CF125C
Swivel Post Clamp, 360°Continuously Adjustable	Thorlabs	SWC
Ø1/2” Optical Post, SS, 8-32 Setscrew, 1/4”-20 Tap, L = 6”	Thorlabs	TR6
Ø1/2” Optical Post, SS, 8-32 Setscrew, 1/4”-20 Tap, L = 3”	Thorlabs	TR3
Large V-Clamp with PM4 Clamping Arm, 2.5” Long	Thorlabs	VC3
Ø1” Pedestal Pillar Post, 1/4”-20 Taps, L = 3”	Thorlabs	RS3P

(*Continued on next page*)

Continued

REAGENT or RESOURCE	SOURCE	IDENTIFIER
Adaptor with External 8-32 Threads and External 1/4''-20 Threads	Thorlabs	AP8E25E
Rotary encoder	U.S. Digital	H5 ball bearing optical shaft encoder
Acrylic disk, 6'' diameter, 1/8'' thick	Amazon	Acrylic disk, 6'' diameter, 1/8'' thick
64 Channel Silicon Probe	Masmanidis Lab, UCLA	64D
Acquisition Board	OpenEphys	Acquisition Board
128 Channel Amplifier Board	Intan Technologies	RHD2000
Arduino Board	Arduino	A000066
I/O Board	OpenEphys	I/O Board
Electroplating Board	Intan Technologies	RHD2000 Electroplating Board
Interface Cable	Intan Technologies	RHD2000 SPI interface Cable
Camera	Thorlabs	DCC1545M
Camera Lens	Thorlabs	MVL50M23
Infrared Illuminator	Towallmark	Towallmark Crazy Cart 48-LED CCTV Ir Infrared Night Vision Illuminator
Patch Clamp Digitizer	Molecular Devices	Multiclamp 700B
Patch Clamp Amplifier	Molecular Devices	Digidata 1550A
Patch Software Suite	Molecular Devices	pCLAMP 10
Capillary Glass Micropipette	Sutter Instruments	BF150-86-10
Micropipette Puller	Sutter Instruments	P-97
Vibratome	Leica	VT1000
LED patterned Illuminator	Mightex	Polygon 400

LEAD CONTACT AND MATERIALS AVAILABILITY

While no unique reagents were generated during this study, requests regarding resources, reagents, and any additional information should be directed to the lead contact, Alexander A Chubykin (Chubykin@purdue.edu). The address for correspondence is 915 W State St, West Lafayette, IN 47907, Department of Biological Sciences, Purdue University

EXPERIMENTAL MODEL AND SUBJECT DETAILS

All animal procedures in this study were approved by Purdue Animal Care and Use Committee (PACUC, protocol number 1408001112). Adult B6.129P2-*Fmr1*tm1Cgr/J (*Fmr1* KO, JAX Stock No. 003025), B6.Cg-Tg(Thy1-COP4/EYFP)18Gfng/J (Thy1-ChR2-YFP, JAX Stock No. 007612), and wild-type (WT) C57/BL6 mice (all strains obtained from JAX) were used as breeders. For *in vivo* extracellular recordings, P60-P65 littermate-controlled WT and *Fmr1* KO male or female (homozygous) mice were used. For *in vitro* CRACM experiments, P35 to P39 littermate-controlled WT and *Fmr*1 KO male mice in the background of heterozygous Thy1-ChR2-YFP were used. These mice were generated from breeding homozygous Thy1-ChR2-YFP females with *Fmr1* KO males.

METHOD DETAILS

Surgical Procedures

The surgical procedures for head-fixed mice follow those previously described. To summarize: Littermate matched C57BL/6 or *Fmr1* KO mice were selected for surgery at ~P55. A head post was implanted, and a headcap formed with metabond™ bone cement under 1.5% inhaled isoflurane anesthesia. The coordinates of the binocular visual cortex (from lambda: AP 0.8 mm, ML ± 3.2 mm) were marked using Neurostar™ stereodrive software. After a day of recovery, awake mice began habituation to the head-fixation apparatus for a minimum of 4 days (90 min/day). For mice that were habituated on a treadmill instead of a stationary (tube) set up, at least 6 days were allowed to ensure they had learned to control the wheel. The apparatus for stationary animals consists of an immobile tube that secures the mouse on a raised platform 16.51 cm directly in front of and centered on a 47.63 cm x 26.99 cm monitor screen and a bar to hold the surgically implanted head post. The apparatus is the same for the mobile setup, with the exception that the animal can freely move on a 6'' diameter vertical treadmill. The majority of the mice in this study were recorded on the treadmill, but 7 WT and 7 FX were included from the stationary set up and were considered immobile as it was not possible for them to run. On the first day of habituation, some mice displayed signs of struggle in order to escape head fixation in the stationary setup. By

the third or fourth day of habituation and during recording sessions, we did not observe these behaviors. Mice also exhibited grooming behavior by the third or fourth day of habituation. On the treadmill, many mice moved cautiously the first 3 days of habituation but could typically run well by day 5 or 6 when they chose to. On the recording day (~P60), a craniotomy was made above the visual cortex of a single hemisphere during ~5min of inhaled anesthesia (1.5% isoflurane) in the stereotaxic apparatus. Mice were then head fixed to the experimental apparatus, and a 64 channel silicon electrode was inserted normal to the surface of the binocular area of the primary visual cortex (AP: 0.8 mm, ML: +/− 3.2 mm, DV +1.0 mm from Lambda). 30 mins was allowed for the animals to fully awaken from anesthesia before recording.

Visual Stimulation

Open source python based psychology software (PsychoPy) was used to present visual stimuli. Control gray screen was created using the color space "gray." The mean luminance of the monitor was 73 cd/m^2. After a day of recovery, mice began habituation to the head-fixation apparatus. During habituation, mice viewed a control gray screen for 90mins per day. Mice were shown single 0.2 s sinusoidal drifting gratings (spatial frequency (SF) = 0.03 cycles per degree of visual angle, temporal frequency (TF) = 3 Hz, speed = 100 deg/s, oriented and drifting at an angle of 150 degrees) for 20 trials in pre-experience recordings for experiments in the immobile setup, or 40 trials for experiments on the treadmill. Gray screen was presented for 0.5 s before stimulus onset to serve as a baseline with a total recording time of 2.5 s for each trial, with an inter-trial interval of 8 s. Mice were then trained to the same stimulus for 4 days. Animals were trained to this stimuli 200 times in 30 mins each day for 4 days. Post-experience recordings included the same visual stimulation paradigm as pre-experience, but with the addition of a novel stimulus in the form of a checkerboard for a subset of mice.

Data Acquisition and Python Packages

Recordings were made using 64 channel silicon probes, 1.05 mm in length, with channels separated 25-50 μm vertically and 16-20 μm horizontally (Shobe et al., 2015). Recordings were made in sets of 20 trials for stationary mice or 40 trials for mice recorded on the treadmill, 4.0 s in duration (later cut to 2.5 s per trial). Raw traces and bandpass filtered units (300 to 6000 Hz) were digitized at 30 kHz and acquired with OpenEphys acquisition hardware and software. Local field potentials (LFP's) were filtered (1-300 Hz) from raw traces post hoc. All data were plotted and analyzed with jupyter notebook using custom Python code written in our laboratory. Open source data analysis libraries including Pandas, Scipy, Matplotlib, Seaborn, and sklearn were used to analyze and plot the data. Pupillometry recordings were acquired with a Thorlabs DCC1545M camera positioned approximately 28.5 cm away from the mouse eye, while the pupil was illuminated with infrared light. The videos were analyzed post hoc.

LFP analysis

Raw traces were down sampled to 1 kHz and manually inspected for artifacts before further analysis. A notch filter was applied to remove 60 Hz noise. LFPs were compared between animals by taking the first and strongest trial averaged (20 trials for stationary mice or 40 trials subdivided into mobile or immobile trials for treadmill mice) visually evoked potential (VEP) elicited after visual stimulation (putative L4 VEPs) from each of the 3 channel columns of the silicon probe, which were then averaged to obtain a single LFP recording per animal. Because the probes were inserted normal to the surface of the cortex, we could ascertain the current source density (CSD) profile of visually evoked responses. CSD analysis was performed on the trial averaged VEPs across the cortical depth using the spline iCSD method in python on a single column of channels on the 64 Ch probe (Aizenman et al., 1996; Łeski et al., 2007; Mitzdorf, 1985; Pettersen et al., 2006). To determine the average amplitudes of the trial averaged VEPs between mice, 4 windows of time were used to capture local minima (VEP1: 0.53-0.63 s, VEP2: 0.73-0.83 s, VEP3: 0.93-1.03 s, VEP4:1.15-1.25 s) corresponding to the VEP timings observed in our recordings. Time-frequency analysis was performed by using complex wavelet convolution on trial averaged L4 VEPs across mice (Cohen, 2015). We used a series of complex wavelets to extract power and phase at each sample point. We used 40 frequencies across a logarithmic range from 2 to 80 Hz, with the number of cycles of the wavelet ranging from 3 to 10 for an optimal time-frequency precision tradeoff. Power was dB normalized to the baseline period. The mean power was then calculated across the Theta (4-8 Hz), Alpha (8-12 Hz), Beta (12-30 Hz), Low Gamma (30-50 Hz), and High Gamma (50-80 Hz) frequency ranges for each animal, and was then used to compare between groups.

Spike detection and sorting

We used Kilosort, a template based clustering algorithm implemented in MATLAB, to detect and sort spikes from raw binary data (Pachitariu et al., 2016). We used the default Kilosort parameters, but set a threshold of 6 SD for spike detection and initialized the templates from data. Clusters were further manually inspected using the Phy template GUI, and several criteria were used to determine the quality of units to be used for further analysis (Rossant et al., 2016) as previously described (Kissinger et al., 2018).

Single unit analysis

Peristimulus time histograms (PSTHs) of single unit activity were computed using 10 ms bins and smoothed with a Gaussian Kernel (width = 100 ms). PSTHs for immobile and mobile trials were created separately, where at least 10 mobile trials had to be present for those trials to be included in the mobile PSTH. All recordings had at least 10 immobile trials. For heatmaps, z-scores were calculated by normalizing to the mean firing rate (FR) across all time (z = (FR – mean FR)/SD. FR). For population time course line plots, z-scores

were calculated by normalizing FR to the baseline period (0-0.5 s)(z = (FR – mean baseline FR)/SD baseline FR). To quantify the duration of oscillations in single units, we applied a peak detection algorithm on the z-transformed PSTH with the following criteria: 1) The minimum peak height must be at least 1.5 SD from baseline, 2) the first peak must be within 100 ms of the stimulus onset, 3) peaks must be within 200 ms from one another. The timing of visual stimulus onset (0.5 s) was then subtracted from the timing of the last detectable peak to ascertain oscillation duration. Units were grouped into different clusters using K-Means, an unsupervised clustering algorithm from the sklearn Python package. The input matrix was the PSTH zscore of single units 0 to 1.2 s after the onset of visual stimulation (the timing window where visually evoked oscillations are observed). We used simple 2-cluster unbiased k-means clustering to separate units into those that were strongly excited during the oscillatory period and those that were not. All units with waveform trough to peak times less than 0.45 were considered putative FS neurons, resulting in ~20%–23% of the visually excited units recorded for each condition being sorted into this category. FX mice had 3%–4% fewer FS cells on average for each condition, though this was not significant.

Directed Information Analysis

Layer-Wise Connection Strength Estimation:

We used a statistical procedure to infer putative connections between units. Connection strength was measured with regularized directed information based on parametric regression models. Those unit-level connection strengths were then aggregated into layer-wise connection strengths.

Spike Train Preprocessing:

For each recording, we only used spikes that occurred between 700 ms (end of stimulus onset) and 1500 ms for each trial to capture the persistent oscillatory period. Time was discretized into 1 ms bins, resulting in binary-valued spike trains for each unit.

Partially-Exhaustive Search for Putative Connections Between Units:

To identify putative connections between units, for each unit Y we used a partially-exhaustive search over all sets of candidate pre-synaptic units from the same recording. If a recording contained few units, then for each unit Y, all sets of up to four other units were examined as sets of candidate pre-synaptic units for Y. Otherwise, all sets of cardinality one were examined, and for cardinality k with $2 \leq k \leq 4$, 10,000 sets of candidate pre-synaptic units with that cardinality were selected based on the best candidates from the $k = 1$ and k-1 searches.

Regressions:

To assess the statistical fit of each set of candidate pre-synaptic units for each unit Y, we modeled Y's activity with a parametric model. The activity Y(t) was regressed using several exogenous variables. Two exogenous variables were for Y's own past, Y(t-1)+Y(t-2), specified to capture the refractory period, and Y(t-3)+…+Y(t-10) to capture self-dependence. One exogenous variable, X(t-1)+…+X(t-10), was used for each unit X in the set of candidate pre-synaptic units. Lastly, a constant was used as an offset. The Markov order of 10 ms and choice of exogenous variables were selected *ad hoc* to balance model simplicity, accuracy, and computational burden. To demonstrate that 10ms is not too limiting of a Markov order, in the supplementary material we include an analysis using a Markov order of 30 ms and obtain comparable results.

For regression, a generalized linear model using the logit link function (logistic regression) was used. For a given unit Y, a set of candidate pre-synaptic units, and a time t, the likelihood of the binary variable Y(t) given the column vector of exogenous variables x and row vector of parameters θ was modeled as

$$P(Y(t) = 1|x;\theta) = \frac{1}{1+e^{-\theta x}} \quad (1)$$

Regression was performed using the GLM fit function for the binomial family in the Statsmodels (v0.9.0) package for Python (v3.7.0) to find maximum likelihood estimates for the parameter vector θ. The time periods [700 ms, 1500 ms] for all the trials were used together for regression. Periods of time with no spikes from Y or candidate pre-synaptic units and for which there were no spikes in the 100 ms prior were not included, to mitigate data imbalance.

Directed Information Calculation:

To measure the strength of candidate connections, we used regularized directed information. Directed information is an information theoretic quantity that measures in bits how well the past of one (or more) time-series predicts the future of another (Marko, 1973). It is a non-parametric generalization of Granger causality (Granger, 1969) using expected cumulative regret with the log-loss function (Quinn et al., 2015). It was independently discovered as transfer entropy (Schreiber, 2000).

For a time-series Y(t) and a (possibly vector-valued) time-series X(t), the directed information from X to Y under joint distribution P(X(1),…,X(T),Y(1),…,Y(T)) with a Markov-order one model is

$$\mathrm{I}(X \to Y) = \frac{1}{T}\sum_{t=1}^{T} \mathrm{E}_P\left[\log_2 \frac{P(Y(t)|Y(t-1),X(t-1))}{P(Y(t)|Y(t-1))}\right] \quad (2)$$

The argument in the sum is also the conditional mutual information$\mathrm{I}(X(t-1);Y(t)|Y(t-1))$

For every recorded unit Y and set of candidate pre-synaptic units, we estimated the directed information. To do so, we used the maximum likelihood estimate of the parameter vector θ for the Markov-order 10 ms model described above and took the empirical

average as an approximation to the statistical average. The empirical average is known to converge to the statistical average for stationary conditional distributions (Quinn et al., 2011).

Minimum Description Length:

To avoid over-fitting and to compare candidate sets of pre-synaptic units with different cardinalities, we regularized the directed information estimates. We used the minimum description length (MDL) complexity penalty for parametric models (Grünwald, 2007). Regularizers for parametric models assist in comparing models with different numbers of parameters and mitigate over-fitting. They balance low model error (low negative log likelihood) and using few parameters (low model complexity). Using MDL, the total complexity of a Markov-order one model P_θ of time-series Y conditioned on its past and the past of time-series X and parameterized by θ is

$$-\frac{1}{T}\sum_{t=1}^{T}\log_2 P_\theta(Y(t)|Y(t-1),X(t-1)) + \frac{|\theta|\log_2 T}{2T}$$

where $|\theta|$ is the number of parameters. We seek the model with the overall lowest complexity. We can compare how well any set X of candidate pre-synaptic units performs compared to the null model (with Y(t) only depending on Y's past) by taking the difference between total complexities, yielding that we seek to maximize

$$\mathrm{I}(X \to Y) - \frac{(|\theta_X| - |\theta_0|)\log_2 T}{2T}$$

where θ_X and θ_0 are the parameter vectors of the candidate and null models, respectively. A value of zero entails that the improvement in modeling the data is the same as would be expected due to overfitting. For each unit Y, this quantity was computed for all sets X of candidate pre-synaptic units using the fitted Markov-order 10 ms models. The set X of candidate pre-synaptic units with the largest value greater than zero was selected as having putative pre-synaptic connections to Y. The values were then normalized by the complexity of Y alone to yield a percentage of how much of unit Y's randomness was reduced by conditioning on the past of X.

Layer-wise Connection Strength Estimation

After computing connection strengths between units and selecting putative connections, we then assigned connection strengths between layers as follows. For each unit Y, we evenly divided the regularized, normalized directed information among Y's putative pre-synaptic units. Thus, each putative connection between a pair of units had a corresponding value for strength. We then aggregated the weights based on layers of the pre-synaptic and post-synaptic units in the putative connections. Thus, for every ordered pair of layers, there was a vector of connection weights from the putative connections between units from these layers.

To assess the overall differences between wild-type and Fragile-X type mice due to perceptual experience, we first computed the median connection weights between each ordered pair of layers. For each ordered pair of layers, we then took the difference between the median weight for those layers using wild-type post-experience data and the median weight for those layers using Fragile-X type post-experience data.

Significance Testing:

Significance was tested using Monte Carlo approximations for two-sided permutation tests. One million iterations were used for every pair of layers for each heatmap in Figure 4. For each iteration, each putative edge from a unit in the pre-synaptic layer to a unit in the post-synaptic layer was relabeled as wild-type or Fragile-X using proportions of possible edges between the corresponding ordered pair of layers. The number of possible edges was calculated based on the number of units in each layer in each WT and FX post-experience recording and the in-degree limit used in the search for putative connections. For each iteration, the medians of non-zero edge strengths were calculated for wild-type and Fragile-X edges, and the difference of the median computed. Monte Carlo approximations were used because some layer-layer pairs had no or few inferred edges in any wild-type or any Fragile-X recordings, precluding the use of standard tests like the Wilcoxon rank-sum test. The Monte Carlo approximations were computed in Python. We then corrected the p values by controlling the false discovery rate using the Benjamini-Hochberg procedure, implemented in the Statsmodels package (Benjamini and Hochberg, 1995). Since there were eight layers, there were 64 layer-layer pairs. With three settings, pre-experience, post-experience, and post-experience with novel stimuli, there were 3*64 = 192 simultaneous hypothesis tests.

Cross Correlation Analysis of Unit Pairs

Cross-correlation analysis is a simple, interpretable procedure to examine statistical correlation between pairs of spike trains over time. It allows for researchers to visually inspect and quantify how likely one unit will have an action potential a short period after another unit does. With appropriate normalization of spiking coincidences between the pair, significance of the observed peaks (for excitation) or troughs (for inhibition) can be measured. We followed standard cross-correlation methods (Dupret et al., 2013). We used 50 ms windows before and after pre-synaptic action potentials, with 1 ms bins. For each pre-synaptic action potential, we counted the number of post-synaptic action potentials within 50 ms before and afterward. We then normalized by the number of pre-synaptic action potentials. We subtracted a baseline rate measured by averaging the 30-50 ms before and after the pre-synaptic action potential. We then identified the highest peak 1-3 ms after the pre-synaptic action potential. The peak height above baseline was interpreted as the spike transmission probability. A significance threshold was set for 3 standard deviations from the baseline.

Pupillometry and Locomotion Analysis

All recordings of mouse pupil size were analyzed post hoc using custom programs written in Python and utilizing the open source computer vision library OpenCV. We imaged the mouse eye at 400 × 300 pixels at 20 Hz with an infrared (IR) camera and lens (Thorlabs). The eye was illuminated with an 850 nm IR LED. (CMVision IR30). Acquired videos were analyzed using the OpenCV library in Python. For each video, the region of interest that only included eye boundaries was selected. For each frame, we first performed image histogram equalization to improve the contrast of the images followed by a Gaussian blur. To perform image segmentation and separate the pupil from the rest of the eye, we applied binary image thresholding. The morphological transformation function morphologyEx was used to remove noise. This was achieved by first using erosion that removes white noise, followed by dilation to restore the original object boundaries, effectively removing white noise. Then we identified the pupil contours by using the function 'findContours' with a mode (RETR_TREE) and method (CHAIN_APPROX_SIMPLE). We used a minimum enclosing circle to define the pupil and to remove edge artifacts caused by whiskers and the IR illumination. Following these procedures, pupil area was extracted. If the eye was not sufficiently illuminated, we could not properly track the pupil and had to exclude those recordings from analysis. All recordings of pupil diameter were baseline normalized and reported as a % change from baseline. Locomotion was acquired using a rotary encoder (U.S. Digital) attached to a custom made treadmill. TTL squarewave outputs from the rotary enoder were sent to both an Arduino board and the OpenEphys data acquisition board. Inputs to Arduino from the rotary encoder were processed at 40Hz. Mobile trials (running faster than 0.5 cm/s from 0.5 to 1.0 s in a trial) were segregated from immobile trials to reveal any differences in stimulus-evoked running, and to determine the influence of locomotion on pupil size.

Ex vivo acute cortical slice preparation

Animals were euthanized the next day after the last day of visual perceptual experience (between P35 and P39). A cocktail of ketamine (100mg/kg body weight) and xylazine (16mg/kg body weight) was intraperitoneally (IP) injected to anesthetize the animal. Then, the animal was trans-cardially perfused with chilled high-sucrose dissection buffer (HSDC) containing (in mM) 75 sucrose, 10 glucose, 87 NaCl, 2.5 KCl, 1.25 NaH2PO4, 25 NaHCO3, 0.5 CaCl2, 7 MgCl2, and 1.3 ascorbic acid. The brain was quickly removed from the skull, the cortices were cut into blocks and super-glued onto the vibratome (Leica VT1000) stage. Brain slices were cut at 300μm thickness in ice-cold HSDB and then transferred into a holding chamber in 32°C artificial cerebral-spinal fluid (ACSF) containing (in mM): 124 NaCl, 3.5 KCl, 1 CaCl2, 0.8 MgCl2, 1.23 NaH2PO4, 26 NaHCO3, and 10 glucose. Brain slices were initially incubated at 32°C for 30min then at room temperature (about 25°C) for 1h or until used for recording. Brain slices were kept for up to 7h after slicing. All HSDB and ACSF used in the above described procedures were aerated with a gas mixture containing 95% oxygen and 5% carbon dioxide to maintain the pH at around 7.4 and oxygen saturation.

Whole-cell patch clamp recording

Whole-cell patch-clamp recording electrodes were pulled from filamented borosilicate glass capillaries (BF150-86-10, Sutter Instruments) using a micropipette puller (P-97, Sutter Instruments) to a resistance of 3.5-7.9 MΩ. The glass electrodes were filled with an internal solution containing (in mM): 20 KCl, 100 K-gluconate, 10 HEPES, 4 MgATP, 0.3 Na2GTP, 7 phosphocreatine, and 0.2% biocytin with pH adjusted to 7.4 and osmolarity adjusted to 300 mOsm. In some experiments, a small amount of 4% w/v Alexa Fluor 594 (A-10438, ThermoFisher Scientific) dissolved in internal solution was back-loaded into the glass electrode to label the patched cell. This dye loading method was described in previous literature. The whole-cell patching procedure was conducted using an image-guided automatic *in vitro* patching system (Autopatcher IG) developed in our lab (Wu and Chubykin, 2017; Wu et al., 2016). The patch clamp recording signal was amplified (Multiclamp 700B) and digitized at 20 kHz sampling rate (Digidata 1550A, Molecular Devices) before being saved to the computer. All raw traces were low-pass filtered at 10 kHz before further analysis.

ChannelRhodopsin-assisted Circuit Mapping (CRACM)

CRACM was conducted in acute *ex vivo* visual cortical slices on a patch-clamp electrophysiology rig. Light stimulation was generated by a high-power LED (470 nm, 50 W, Mightex). The stimulation pattern was generated by an LED patterned illuminator (Polygon 400, Mightex) and projected onto the brain slice via a 10x objective lens (Avants et al., 2015). The total area scanned for each map is 0.67 mm by 0.67 mm, which is divided into 10x10 grid. Each stimulus (one pixel) is 10 ms in length, with a 2 s inter-stimulus interval. The power coming out of the objective was 0.3 mW for a 10 ms stimulus, as measured by a digital power meter (Thorlabs PM121D). The stimulation sequence was a pre-defined pseudo-random sequence, which avoids surrounding inhibition from scanning in sequence. All CRACM recordings were conducted under voltage-clamp mode with a −70 mV holding potential. LED stimulation patterns were designed and controlled with the manufacture's software. Stimulation and recording were synchronized by the patch-clamp digitizer. Cell averaged CRACM maps were constructed by averaging the pixel values between cells in each experimental group, with the soma positioned in the center of each map.

Perfusions, Histology and Imaging

Mice were perfused with 1xPBS, followed by 4% PFA. After extraction, the brain was stored in 4% PFA for 24-48 hr before making 100 μm thick coronal sections on a vibrating microtome (1000 Plus, Vibratome). Some slices were counter stained (free floating) with DAPI in PBS. Slices were mounted onto glass slides with anti-fading mounting media containing n-propyl-gallate and sealed with transparent nail polish. The electrode track was then visualized by light microscopy (VWR) to verify the electrode placement in

V1, according to landmarks shown in a mouse brain reference atlas (Neurostar stereotaxic mouse brain atlas, Allen mouse brain atlas). Acute brain slices from *ex vivo* patch clamp recordings were fixed in 4%PFA for 30min to 1h then made into microscopic slides. Images were obtained with confocal microscopy (Zeiss 710).

QUANTIFICATION AND STATISTICAL ANALYSIS

The statistical details for each experiment can be found in the figure legends. Much of our statistical analysis was performed in Python. We used two sample Kolmogorov-Smirnov (KS) tests in Python (Scipy library) to compare the distributions of oscillation durations among populations of single units. These tests were also used to compare the distributions of the peak response oscillation frequency among single units. To account for unequal variance and unequal numbers of units between comparisons, we used a Welch's two sample t test in Python to compare the mean oscillation durations between two unit populations. The Welch's test was also used to compare firing rates at different oscillatory cycles between WT and FX mice, and the mean frequency of peak oscillatory activity among single units. A Mann-Whitney-U test was used to compare the mean baseline normalized power of different frequency bands from LFP recordings, as well as the raw amplitudes of responses at different oscillatory cycles. The mean firing rates of units during mobile or immobile trials were compared using the Wilcoxon-signed rank test. We also analyzed the cumulative distributions of single values averaged across the entire CRACM map for each cell, but this did not yield significance for any comparison when performing a Kolmogorov-Smirnov test. To compare the average EPSC strength (bar graphs in Figures 5 and 6), all EPSCs across the CRACM map for each cell were averaged into single values for comparison between experimental groups. If these data were not normally distributed, we then applied either a log transformation or Box-Cox transformation (Lambda = −1.3614 for L5-L4RS, −0.245 for L5-L5 RS) and performed a two way ANOVA followed by the Tukey test in python. We also performed non-parametric tests (Mann-Whitney U test) for these comparisons and obtained similar results. We have also performed averaging of the top 10 largest values to acquire one value for each CRACM heatmap for these comparisons and obtained similar results. We used a combined D'Agostino and Pearson's normality test from Python SciPy library to test the normality of a distribution. We used a repeated-measures ANOVA in MATLAB to compare optogenetic input-output curves and I-V curves between genotypes. To compare the LFP amplitudes or firing rates at four individual oscillation cycles between WT and FX, we used linear mixed models (LMM) using SAS software followed by the testing of the least-squares (LS) means of fixed effects. Our model contained genotype and cycles as fixed effects along with a mouse/unit as a random effect. Since LMM is a linear model, it shares similar assumptions as ANOVA. We used SAS to fit the model to our data. We tried different transformations of our dependent variable and found that taking the rectified LFP and firing rate to the power of 0.4 gave us the best results (normal residuals). For post hoc tests, we used simple effect comparisons using least-squares means of fixed effects to test for differences between groups at each cycle. P values were then manually corrected by the Bonferroni method.

DATA AND CODE AVAILABILITY

Data and code are available from the corresponding author on a reasonable request.

Cell Reports, Volume *31*

Supplemental Information

Visual Experience-Dependent Oscillations and Underlying Circuit Connectivity Changes Are Impaired in *Fmr1* KO Mice

Samuel T. Kissinger, Qiuyu Wu, Christopher J. Quinn, Adam K. Anderson, Alexandr Pak, and Alexander A. Chubykin

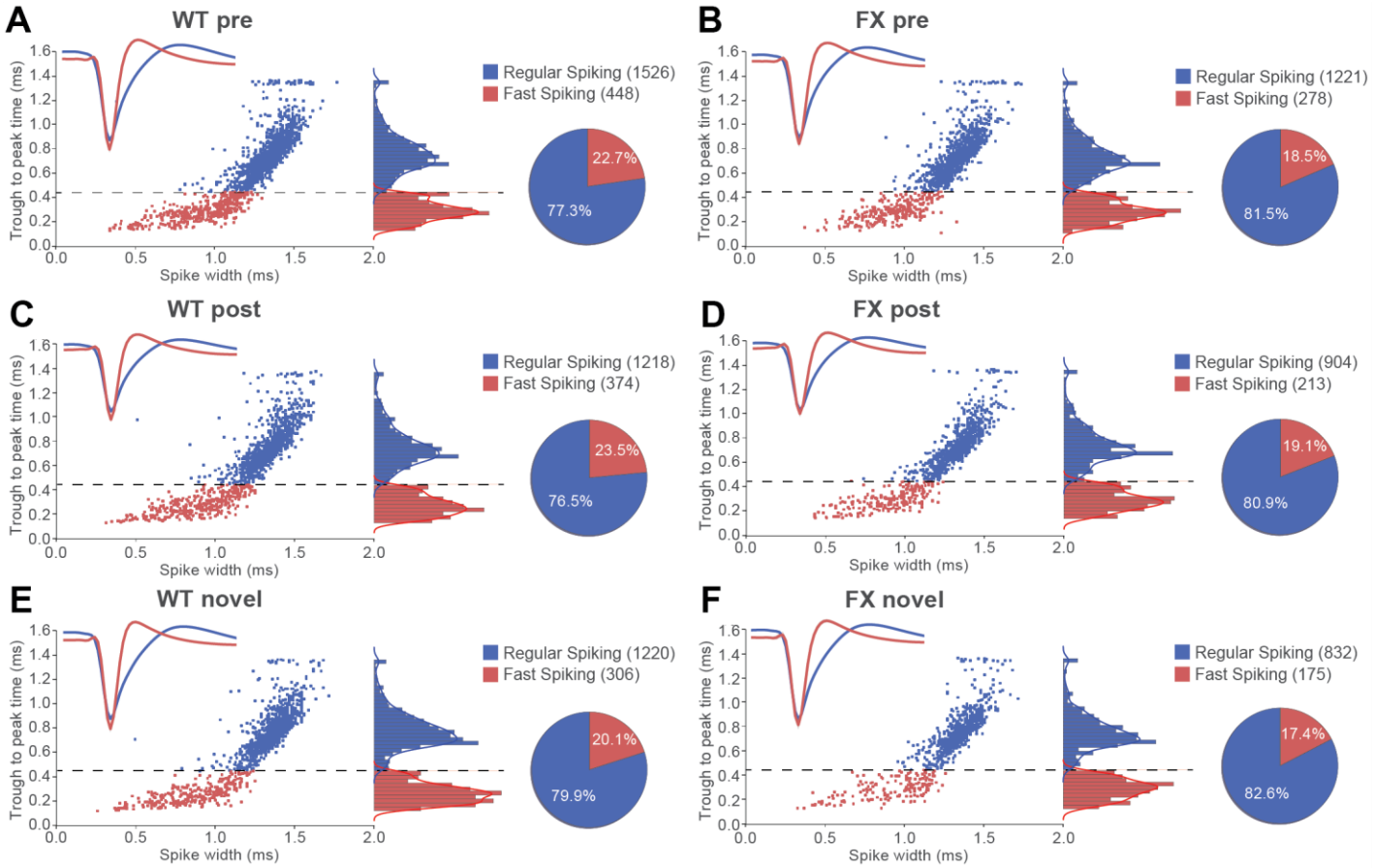

Figure S1. Segregation of regular and fast spiking cells in WT and FX mice for each stimulus condition. Related to Figure 2.

(A) Averaged waveforms, scatterplots and distributions of waveform trough to peak vs spike width times, and pie graphs of the percentage of each neural subtype recorded before the perceptual experience in WT animals. 448 units (22.7%) were FS, while 1526 (77.3%) were RS, across 33 mice.

(B) Units recorded in FX animals pre perceptual experience. FS: 278 (18.5%), RS: 1221 (81.5%) across 25 mice.

(C) Units recorded in WT animals post perceptual experience. FS: 374 (23.5%), RS: 1218 (76.5%) across 31 mice.

(D) Units recorded in FX animals post perceptual experience. FS: 213 (19.1%), RS: 904 (80.9%) across 25 mice.

(E) Units recorded in WT animals in response to novel stimuli. FS: 306 (20.1%), RS: 1220 (79.9%) across 24 mice.

(F) Units recorded in FX animals in response to novel stimuli. FS: 175 (17.4%), RS:832 (82.6%) across 18 mice.

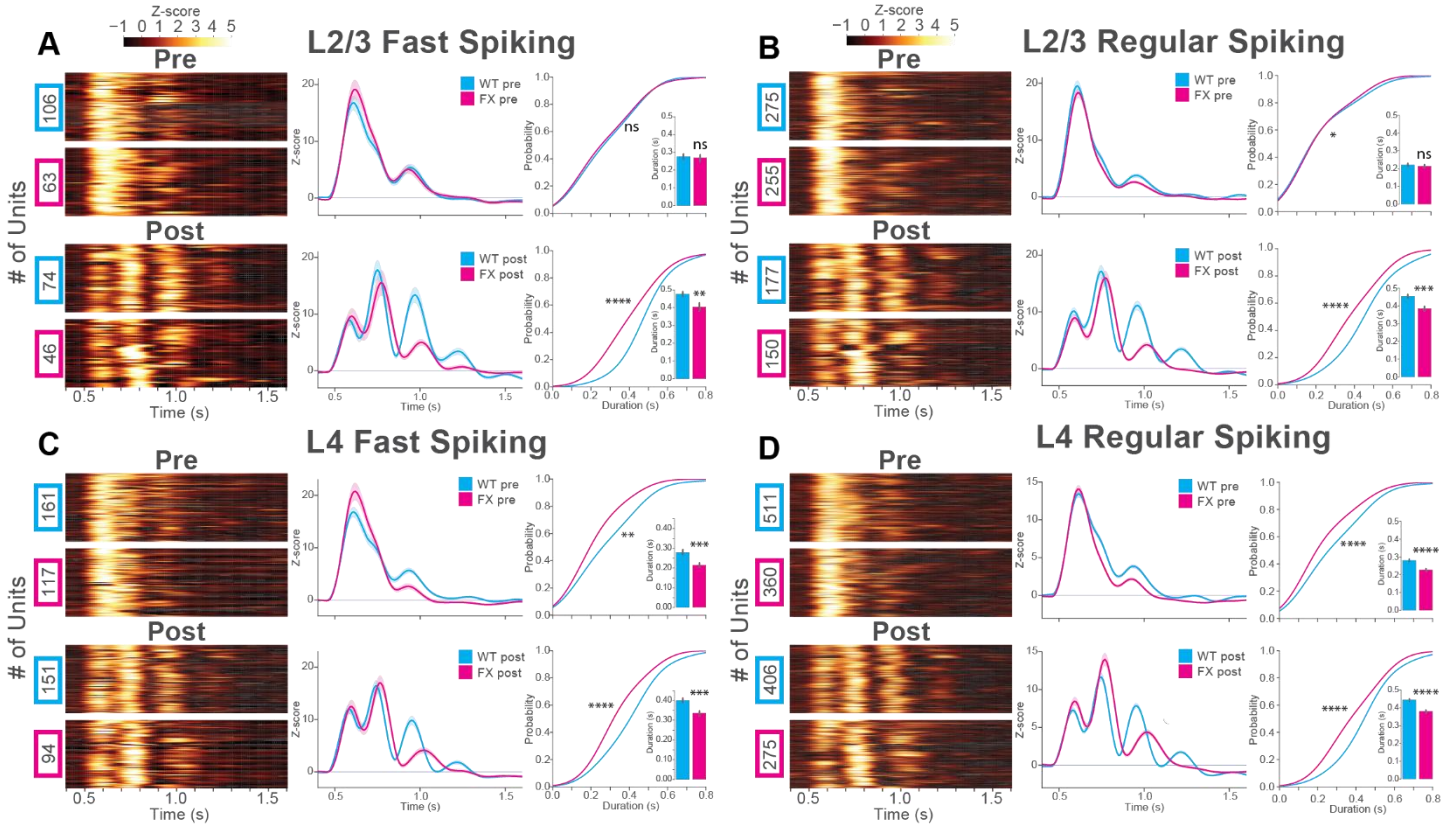

Figure S2. Decreased oscillation duration of regular and fast spiking units in layers 2/3 and 4 of FX mice. Related to Figure 2.

Visually excited units in L2/3 and L4 before and after perceptual experience to grating stimuli. WT (Cyan) 33 mice pre, 31 mice post. FX (magenta) 25 mice pre, 25 mice post. Z-scored firing rates are shown in the heatmaps. Population z-score line plots are shown to the right of the heatmaps. A cumulative distribution (CDF) of oscillation duration is shown to the right of the line plots, with bar graphs of the mean oscillation duration inset.

(A) L2/3 FS units: 2 sample KS test of duration CDFs, pre, WT vs FX duration: D(159)=0.08, p=0.92. Welch's t-test of mean duration: t(159)=0.27, p=0.78 (units after peak detection: WT pre N=101, FX pre N=60). 2 sample KS test of duration CDFs, post, WT vs FX duration: D(115)=0.41, p=9.05E-9. Welch's unequal variances t-test of mean duration:, t(115)=2.66, p=9.33E-3 (units after peak detection: WT post N=72, FX post N=45). Error bars indicate SEM. *p<0.05, **p<0.01,***p<0.001, ****p<0.0001.

(B) L2/3 RS units: 2 sample KS test of duration CDFs, pre, WT vs FX duration: D(501)=0.14, p=0.01. Welch's t-test of mean duration:, t(501)=0.45, p=0.65. (units after peak detection: WT pre N=264, FX pre N=239). 2 sample KS test of duration CDFs, post, WT vs FX duration: D(311)=0.35, p=3.15E-9. Welch's unequal variances t-test of mean duration: t(311)=3.88, p=1.2E-4 (units after peak detection: WT post N=172, FX post N=139.).

(C) L4 FS units: 2 sample KS test of duration CDFs, pre, WT vs FX duration: D(267)=0.22, p=1.89E-3. Welch's t-test of mean duration: t(267)=3.57, p=4.17E-4 (units after peak detection: WT pre N=154, FX pre N=115). 2 sample KS test of duration CDFs, post, WT vs FX duration: D(234)=0.37, p=1.16E-7. Welch's unequal variances t-test of mean duration:, t(234)=3.84, p=1.59E-4 (units after peak detection: WT post N=145, FX post N=91).

(D) L4 RS units: 2 sample KS test of duration CDFs, pre, WT vs FX duration: D(825)=0.17, p=8.20E-6 (units after peak detection: WT pre N=460, FX pre N=367). Welch's unequal variances t-test of mean duration: t(825)=4.85, p=1.42E-6. (2 sample KS test of duration CDFs, post, WT vs FX duration: D(714)=0.35, p=5.32E-17. Welch's t-test of mean duration: t(714)=5.53, p=4.87E-8 (units after peak detection: WT post N=408, FX post N=308).

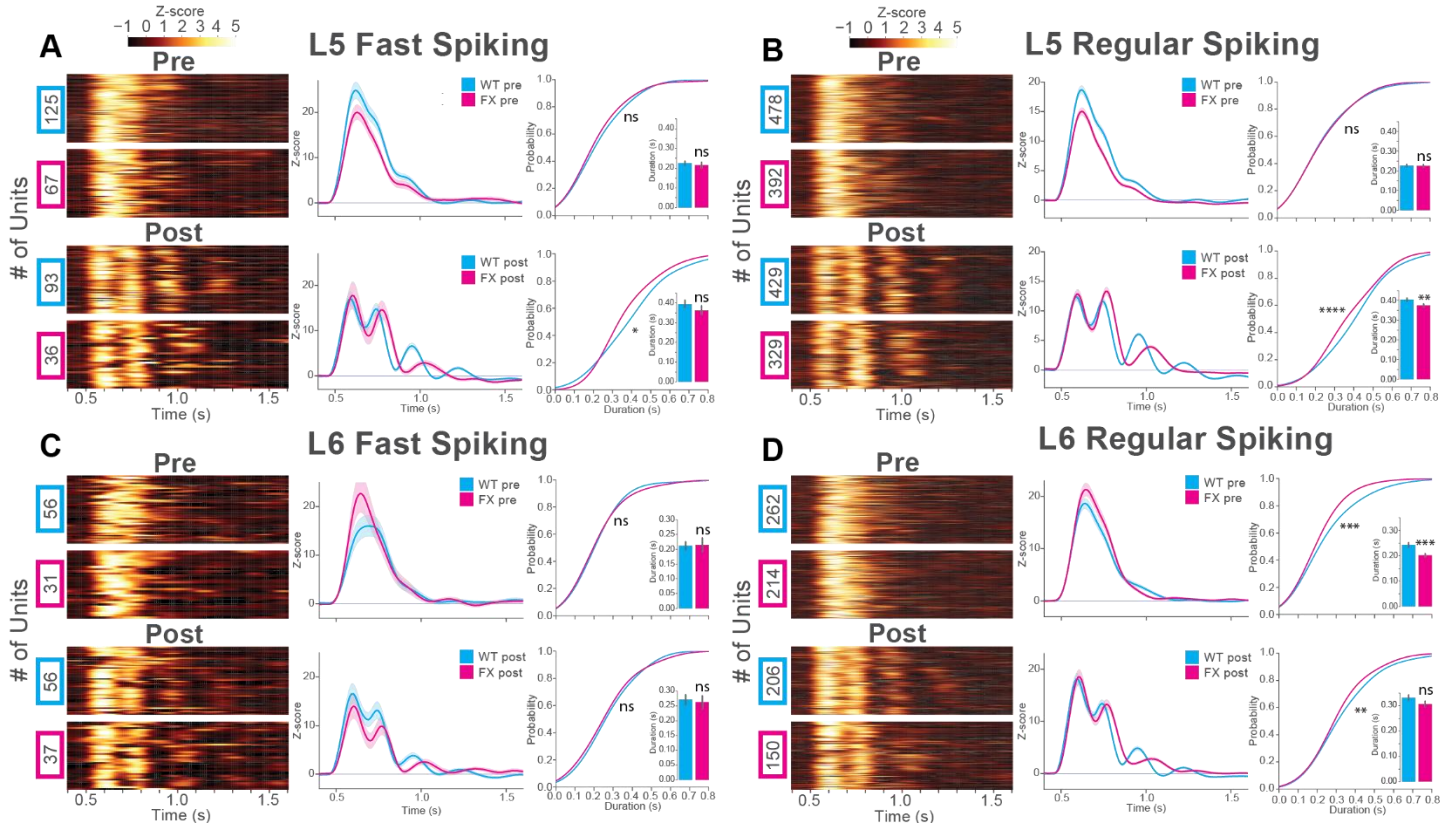

Figure S3. Decreased oscillation duration of regular and fast spiking units in layer 5 and regular spiking units in layer 6 of FX mice after perceptual experience. Related to Figure 2.

Visually excited units in L5 and L6 before and after perceptual experience to grating stimuli. WT (Cyan) 33 mice pre, 31 mice post. FX (magenta) 25 mice pre, 25 mice post. Z-scored firing rates are shown in the heatmaps. Population z-score line plots are shown to the right of the heatmaps. A cumulative distribution (CDF) of oscillation duration is shown to the right of the line plots, with bar graphs of the mean oscillation duration inset.

(A) L5 FS units: 2 sample KS test of duration CDFs, pre, WT vs FX duration: D(190)=0.10, p=0.71. Welch's t-test of mean duration: t(190)=0.49, p=0.62 (units after peak detection: WT pre N=124, FX pre N=66). 2 sample KS test of duration CDFs, post, WT vs FX duration: D(124)=0.27, p=0.03. Welch's unequal variances t-test of mean duration:, t(124)=-1.03, p=0.30 (units after peak detection: WT post N=91, FX post N=35). Error bars indicate SEM. *p<0.05, **p<0.01,***p<0.001, ****p<0.0001.

(B) L5 RS units: 2 sample KS test of duration CDFs, pre, WT vs FX duration: D(825)=0.04, p=0.83. Welch's t-test of mean duration: t(825)=0.12, p=0.90 (units after peak detection: WT pre N=460, FX pre N=367). 2 sample KS test of duration CDFs, post, WT vs FX duration: D(714)=0.23, p=4.74E-9. Welch's unequal variances t-test of mean duration:, t(714)=2.61, p=9.19E-3 (units after peak detection: WT post N=408, FX post N=308).

(C) L6 FS units: 2 sample KS test of duration CDFs, pre, WT vs FX duration: D(83)=0.13, p=0.85. Welch's t-test of mean duration: t(83)=-0.11, p=0.91 (units after peak detection: WT pre N=55, FX pre N=30). 2 sample KS test of duration CDFs, post, WT vs FX duration: D(90)=0.24, p=0.10. Welch's unequal variances t-test of mean duration:, t(90)=0.29, p=0.76 (units after peak detection: WT post N=55, FX post N=37).

(D) L6 RS units: 2 sample KS test of duration CDFs, pre, WT vs FX duration: D(255)=0.15, p=6.94E-3. Welch's t-test of mean duration: t(255)=3.40, p=7.13E-4 (units after peak detection: WT pre N=250, FX pre N=207). 2 sample KS test of duration CDFs, post, WT vs FX duration: D(337)=0.20, p=2.13E-3. Welch's unequal variances t-test of mean duration:, t(337)=1.59, p=0.11 (units after peak detection: WT post N=197, FX post N=142).

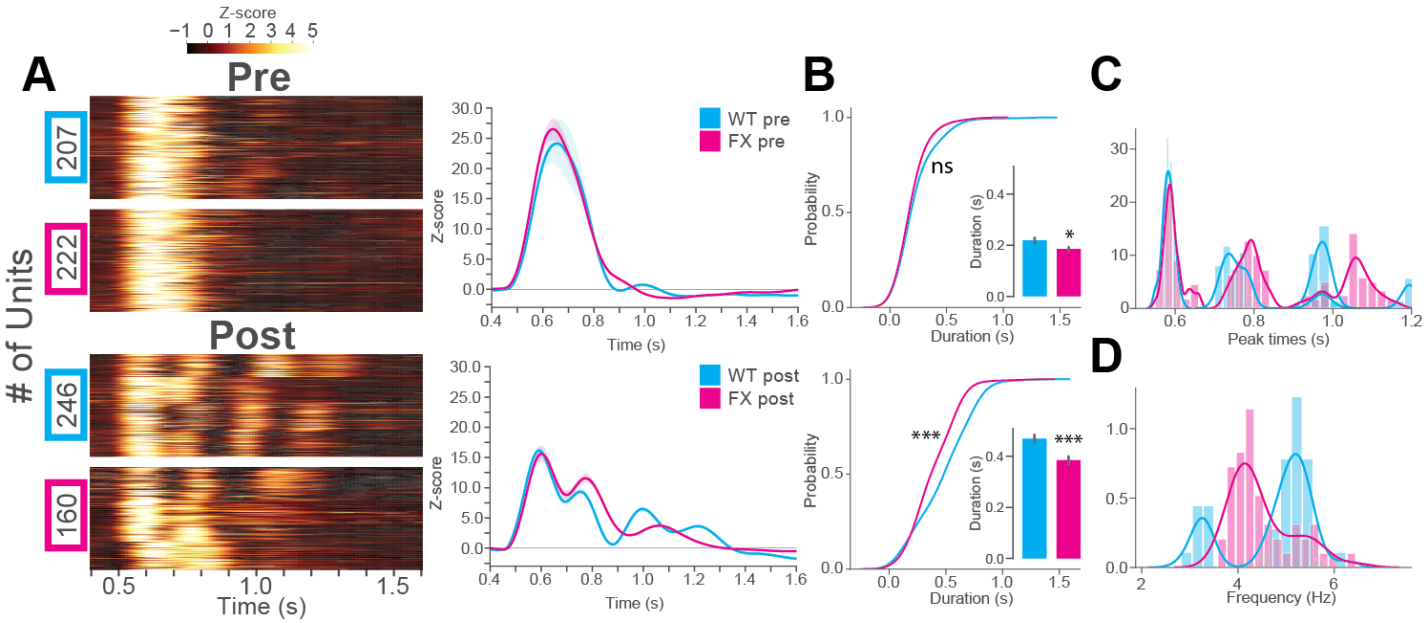

Figure S4. Decreased oscillation durations after perceptual experience in homozygous female FX mice. Related to Figure 2.

(A) Visually excited units across all layers before or after perceptual experience to grating stimuli. WT (Cyan) 4 mice pre, 4 mice post. FX (magenta) 4 mice pre, 4 mice post. Z-scored firing rates are shown in the heatmaps. Population z-score line plots are shown to the right of the heatmaps.

(B) Cumulative distributions (CDF) of oscillation duration, with bar graphs of the mean oscillation duration inset. 2 sample KS test of duration CDFs, pre, WT vs FX duration: $D(427)=0.11$, $p=0.10$. Welch's t-test of mean duration: $t(427)=2.46$, $p=1.42E-2$ (units after peak detection: WT pre N=195, FX pre N=216). 2 sample KS test of duration CDFs, post, WT vs FX duration: $D(404)=0.28$, $p=6.39E-7$. Welch's unequal variances t-test of mean duration:, $t(404)=3.76$, $p=1.96E-4$ (units after peak detection: WT post N=225, FX post N=144). Error bars indicate SEM. *p<0.05, **p<0.01,***p<0.001.

(C) Distributions of peak times across WT and FX unit populations at 3 oscillation cycles for the units in A and B.

(D) Distributions of oscillation frequency for the units in A and B.

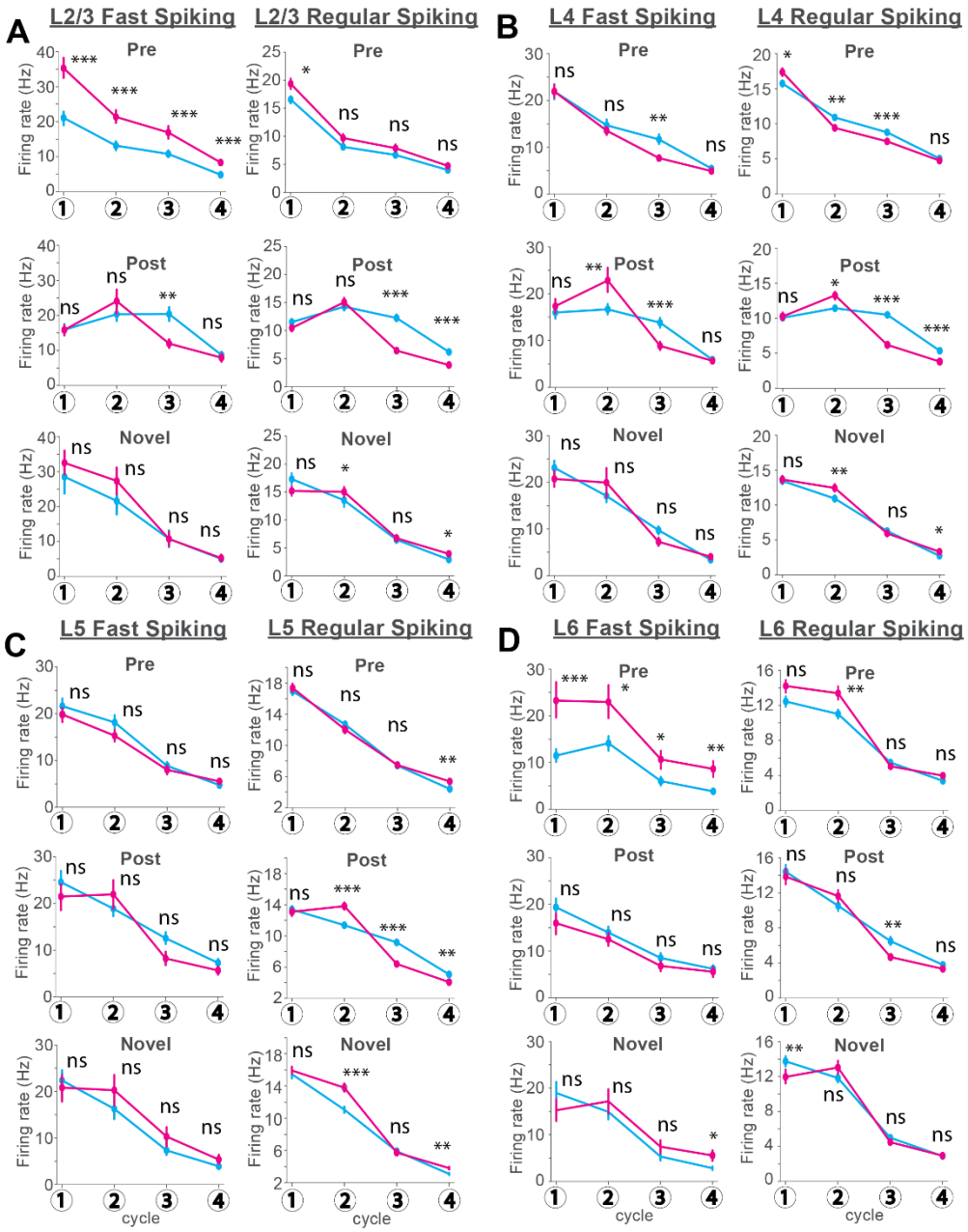

Figure S5. Mean firing rates at each oscillation cycle in WT and FX mice. Related to Figure 2.

(A) Firing rates for L2/3 RS and FS cells at each oscillation cycle and stimulus condition. The units used for this analysis are found in figure S2A and B. See table S1 for statistical analysis. Error bars indicate SEM. *p<0.05, **p<0.01,***p<0.001.

(B) Firing rates for L4 RS and FS cells at each oscillation cycle and stimulus condition. The units used for this analysis are found in figure S2C and D. See table S1 for statistical analysis.

(C) Firing rates for L5 RS and FS cells at each oscillation cycle and stimulus condition. The units used for this analysis are found in figure S3A and B. See table S1 for statistical analysis.

(D) Firing rates for L6 RS and FS cells at each oscillation cycle and stimulus condition. The units used for this analysis are found in figure S3C and D. See table S1 for statistical analysis.

Table S1. Mean firing rates at each oscillation cycle, WT vs FX. Related to Figure 2					
Comparison	**Estimate**	**Standard Error**	**DF**	**t or F**	**p**
Pre L2/3 FS					
Fixed Effect: Genotype	N/A	N/A	167	22.56	<.0004
Fixed Effect: Oscillation number	N/A	N/A	501	242.13	<.0004
Fixed Effect: Group * Oscillation	N/A	N/A	501	3.27	0.021
Pre L2/3 FS Cycle 1	0.8283	0.1502	277.4	5.52	<.0004
Pre L2/3 FS Cycle 2	0.6506	0.1502	277.4	4.33	<.0004
Pre L2/3 FS Cycle 3	0.503	0.1502	277.4	3.35	0.0009
Pre L2/3 FS Cycle 4	0.5119	0.1502	277.4	3.41	0.0007
Pre L2/3 RS					
Fixed Effect: Genotype	N/A	N/A	528	3.49	0.0625
Fixed Effect: Oscillation number	N/A	N/A	1584	836.97	<.0004
Fixed Effect: Group * Oscillation	N/A	N/A	1584	0.88	0.452
Pre L2/3 RS Cycle 1	0.1607	0.07027	929.9	2.29	0.0224
Pre L2/3 RS Cycle 2	0.1049	0.07027	929.9	1.49	0.1357
Pre L2/3 RS Cycle 3	0.06649	0.07027	929.9	0.95	0.3443
Pre L2/3 RS Cycle 4	0.1188	0.07027	929.9	1.69	0.0914
Pre L4 FS					
Fixed Effect: Genotype	N/A	N/A	276	0.02	0.8807
Fixed Effect: Oscillation number	N/A	N/A	828	407.7	<.0004
Fixed Effect: Group * Oscillation	N/A	N/A	828	9.97	<.0004
Pre L4 FS Cycle 1	0.1218	0.1103	451	1.1	0.2698
Pre L4 FS Cycle 2	0.103	0.1103	451	0.93	0.3508
Pre L4 FS Cycle 3	-0.2939	0.1103	451	-2.66	0.008
Pre L4 FS Cycle 4	0.01084	0.1103	451	0.1	0.9217
Pre L4 RS					
Fixed Effect: Genotype	N/A	N/A	869	2.13	0.1452
Fixed Effect: Oscillation number	N/A	N/A	2607	1283.71	<.0004
Fixed Effect: Group * Oscillation	N/A	N/A	2607	23.6	<.0004
Pre L4 RS Cycle 1	0.12	0.04944	1444	2.43	0.0153
Pre L4 RS Cycle 2	-0.1607	0.04944	1444	-3.25	0.0012
Pre L4 RS Cycle 3	-0.1684	0.04944	1444	-3.41	0.0007
Pre L4 RS Cycle 4	-0.04283	0.04944	1444	-0.87	0.3864
Pre L5 FS					
Fixed Effect: Genotype	N/A	N/A	190	0.01	0.9302
Fixed Effect: Oscillation number	N/A	N/A	570	267.36	<.0004
Fixed Effect: Group * Oscillation	N/A	N/A	570	2.51	0.058
Pre L5 FS Cycle 1	-0.03074	0.1344	344.2	-0.23	0.8192
Pre L5 FS Cycle 2	-0.1065	0.1344	344.2	-0.79	0.4287
Pre L5 FS Cycle 3	-0.0801	0.1344	344.2	-0.6	0.5515
Pre L5 FS Cycle 4	0.1771	0.1344	344.2	1.32	0.1883
Pre L5 RS					
Fixed Effect: Genotype	N/A	N/A	868	0.4	0.5255
Fixed Effect: Oscillation number	N/A	N/A	2604	1230.74	<.0004
Fixed Effect: Group * Oscillation	N/A	N/A	2604	7.19	<.0004
Pre L5 RS Cycle 1	0.01396	0.05165	1622	0.27	0.7869
Pre L5 RS Cycle 2	-0.06625	0.05165	1622	-1.28	0.1998
Pre L5 RS Cycle 3	0.02132	0.05165	1622	0.41	0.6799
Pre L5 RS Cycle 4	0.1417	0.05165	1622	2.74	0.0061
Pre L6 FS					
Fixed Effect: Genotype	N/A	N/A	85	10.96	0.0014
Fixed Effect: Oscillation number	N/A	N/A	255	95.91	<.0004
Fixed Effect: Group * Oscillation	N/A	N/A	255	1.74	0.1596
Pre L6 FS Cycle 1	0.8063	0.2064	136.5	3.91	0.0001
Pre L6 FS Cycle 2	0.5297	0.2064	136.5	2.57	0.0114
Pre L6 FS Cycle 3	0.4658	0.2064	136.5	2.26	0.0256
Pre L6 FS Cycle 4	0.6101	0.2064	136.5	2.96	0.0037
Pre L6 RS					
Fixed Effect: Genotype	N/A	N/A	474	2.5	0.1147
Fixed Effect: Oscillation number	N/A	N/A	1422	670.39	<.0004
Fixed Effect: Group * Oscillation	N/A	N/A	1422	6.81	0.0004
Pre L6 RS Cycle 1	0.1289	0.06601	947.8	1.95	0.0511
Pre L6 RS Cycle 2	0.1814	0.06601	947.8	2.75	0.0061
Pre L6 RS Cycle 3	-0.07556	0.06601	947.8	-1.14	0.2526
Pre L6 RS Cycle 4	0.1101	0.06601	947.8	1.67	0.0957

Post L2/3 FS					
Fixed Effect: Genotype	N/A	N/A	118	0.33	0.5651
Fixed Effect: Oscillation number	N/A	N/A	354	86.79	<.0004
Fixed Effect: Group * Oscillation	N/A	N/A	354	11.3	<.0004
Post L2/3 FS Cycle 1	0.1053	0.1738	198.3	0.61	0.5454
Post L2/3 FS Cycle 2	0.1646	0.1738	198.3	0.95	0.345
Post L2/3 FS Cycle 3	-0.5649	0.1738	198.3	-3.25	0.0014
Post L2/3 FS Cycle 4	-0.05445	0.1738	198.3	-0.31	0.7545
Post L2/3 RS					
Fixed Effect: Genotype	N/A	N/A	325	16.35	<.0004
Fixed Effect: Oscillation number	N/A	N/A	975	300.33	<.0004
Fixed Effect: Group * Oscillation	N/A	N/A	975	36.09	<.0004
Post L2/3 RS Cycle 1	-0.0958	0.07581	667.5	-1.26	0.2068
Post L2/3 RS Cycle 2	0.05196	0.07581	667.5	0.69	0.4934
Post L2/3 RS Cycle 3	-0.6408	0.07581	667.5	-8.45	<.0004
Post L2/3 RS Cycle 4	-0.3201	0.07581	667.5	-4.22	<.0004
Post L4 FS					
Fixed Effect: Genotype	N/A	N/A	243	0.05	0.8206
Fixed Effect: Oscillation number	N/A	N/A	729	237.28	<.0004
Fixed Effect: Group * Oscillation	N/A	N/A	729	21.81	<.0004
Post L4 FS Cycle 1	0.1206	0.1204	424.9	1	0.317
Post L4 FS Cycle 2	0.3614	0.1204	424.9	3	0.0028
Post L4 FS Cycle 3	-0.4271	0.1204	424.9	-3.55	0.0004
Post L4 FS Cycle 4	0.03915	0.1204	424.9	0.33	0.7451
Post L4 RS					
Fixed Effect: Genotype	N/A	N/A	679	12.79	0.0004
Fixed Effect: Oscillation number	N/A	N/A	2037	510.45	<.0004
Fixed Effect: Group * Oscillation	N/A	N/A	2037	65.31	<.0004
Post L4 RS Cycle 1	-0.01959	0.05341	1321	-0.37	0.7139
Post L4 RS Cycle 2	0.1334	0.05341	1321	2.5	0.0126
Post L4 RS Cycle 3	-0.4951	0.05341	1321	-9.27	<.0004
Post L4 RS Cycle 4	-0.2558	0.05341	1321	-4.79	<.0004
Post L5 FS					
Fixed Effect: Genotype	N/A	N/A	127	0.3	0.5836
Fixed Effect: Oscillation number	N/A	N/A	381	119.65	<.0004
Fixed Effect: Group * Oscillation	N/A	N/A	381	4.34	0.0051
Post L5 FS Cycle 1	-0.06021	0.2048	215.4	-0.29	0.7691
Post L5 FS Cycle 2	0.1995	0.2048	215.4	0.97	0.3312
Post L5 FS Cycle 3	-0.3931	0.2048	215.4	-1.92	0.0563
Post L5 FS Cycle 4	-0.1374	0.2048	215.4	-0.67	0.5031
Post L5 RS					
Fixed Effect: Genotype	N/A	N/A	756	3.95	0.0472
Fixed Effect: Oscillation number	N/A	N/A	2268	821.28	<.0004
Fixed Effect: Group * Oscillation	N/A	N/A	2268	53.89	<.0004
Post L5 RS Cycle 1	-0.0331	0.04897	1515	-0.68	0.4993
Post L5 RS Cycle 2	0.2123	0.04897	1515	4.33	<.0004
Post L5 RS Cycle 3	-0.3468	0.04897	1515	-7.08	<.0004
Post L5 RS Cycle 4	-0.1541	0.04897	1515	-3.15	0.0017
Post L6 FS					
Fixed Effect: Genotype	N/A	N/A	91	2.11	0.1502
Fixed Effect: Oscillation number	N/A	N/A	273	100.09	<.0004
Fixed Effect: Group * Oscillation	N/A	N/A	273	0.37	0.7744
Post L6 FS Cycle 1	-0.2772	0.1718	161.1	-1.61	0.1086
Post L6 FS Cycle 2	-0.1757	0.1718	161.1	-1.02	0.308
Post L6 FS Cycle 3	-0.255	0.1718	161.1	-1.48	0.1398
Post L6 FS Cycle 4	-0.1476	0.1718	161.1	-0.86	0.3915
Post L6 RS					
Fixed Effect: Genotype	N/A	N/A	354	1	0.3188
Fixed Effect: Oscillation number	N/A	N/A	1062	554.12	<.0004
Fixed Effect: Group * Oscillation	N/A	N/A	1062	6.66	0.0002
Post L6 RS Cycle 1	-0.07444	0.07315	691.9	-1.02	0.3092
Post L6 RS Cycle 2	0.08321	0.07315	691.9	1.14	0.2557
Post L6 RS Cycle 3	-0.2106	0.07315	691.9	-2.88	0.0041
Post L6 RS Cycle 4	-0.04135	0.07315	691.9	-0.57	0.572
Novel L2/3 FS					
Fixed Effect: Genotype	N/A	N/A	48	0.97	0.3284
Fixed Effect: Oscillation number	N/A	N/A	144	94.36	<.0004
Fixed Effect: Group * Oscillation	N/A	N/A	144	1.63	0.1853

Novel L2/3 FS Cycle 1	0.4536	0.3105	87.27	1.46	0.1476
Novel L2/3 FS Cycle 2	0.4836	0.3105	87.27	1.56	0.123
Novel L2/3 FS Cycle 3	0.06215	0.3105	87.27	0.2	0.8418
Novel L2/3 FS Cycle 4	0.0443	0.3105	87.27	0.14	0.8869
Novel L2/3 RS					
Fixed Effect: Genotype	N/A	N/A	211	1.78	0.1842
Fixed Effect: Oscillation number	N/A	N/A	633	427.35	<.0004
Fixed Effect: Group * Oscillation	N/A	N/A	633	5.53	0.0009
Novel L2/3 RS Cycle 1	-0.09733	0.1018	435.5	-0.96	0.3395
Novel L2/3 RS Cycle 2	0.2024	0.1018	435.5	1.99	0.0475
Novel L2/3 RS Cycle 3	0.07667	0.1018	435.5	0.75	0.4518
Novel L2/3 RS Cycle 4	0.2622	0.1018	435.5	2.58	0.0103
Novel L4 FS					
Fixed Effect: Genotype	N/A	N/A	214	0.33	0.5674
Fixed Effect: Oscillation number	N/A	N/A	642	364.85	<.0004
Fixed Effect: Group * Oscillation	N/A	N/A	642	4.5	0.0039
Novel L4 FS Cycle 1	-0.162	0.1317	386.7	-1.23	0.2195
Novel L4 FS Cycle 2	0.03545	0.1317	386.7	0.27	0.788
Novel L4 FS Cycle 3	-0.2468	0.1317	386.7	-1.87	0.0618
Novel L4 FS Cycle 4	0.116	0.1317	386.7	0.88	0.3792
Novel L4 RS					
Fixed Effect: Genotype	N/A	N/A	613	1.82	0.1774
Fixed Effect: Oscillation number	N/A	N/A	1839	1185.15	<.0001
Fixed Effect: Group * Oscillation	N/A	N/A	1839	6.3	0.0003
Novel L4 RS Cycle 1	0.01919	0.05428	1189	0.35	0.7237
Novel L4 RS Cycle 2	0.1449	0.05428	1189	2.67	0.0077
Novel L4 RS Cycle 3	-0.04013	0.05428	1189	-0.74	0.4599
Novel L4 RS Cycle 4	0.1207	0.05428	1189	2.22	0.0264
Novel L5 FS					
Fixed Effect: Genotype	N/A	N/A	130	1.39	0.241
Fixed Effect: Oscillation number	N/A	N/A	390	186.5	<.0001
Fixed Effect: Group * Oscillation	N/A	N/A	390	3.73	0.0115
Novel L5 FS Cycle 1	-0.08649	0.1845	208.6	-0.47	0.6397
Novel L5 FS Cycle 2	0.3493	0.1845	208.6	1.89	0.0597
Novel L5 FS Cycle 3	0.2886	0.1845	208.6	1.56	0.1193
Novel L5 FS Cycle 4	0.2158	0.1845	208.6	1.17	0.2435
Novel L5 RS					
Fixed Effect: Genotype	N/A	N/A	793	7.93	0.005
Fixed Effect: Oscillation number	N/A	N/A	2379	1605.3	<.0001
Fixed Effect: Group * Oscillation	N/A	N/A	2379	11.82	<.0001
Novel L5 RS Cycle 1	0.07126	0.04965	1557	1.44	0.1514
Novel L5 RS Cycle 2	0.2546	0.04965	1557	5.13	<.0001
Novel L5 RS Cycle 3	-0.00285	0.04965	1557	-0.06	0.9543
Novel L5 RS Cycle 4	0.142	0.04965	1557	2.86	0.0043
Novel L6 FS					
Fixed Effect: Genotype	N/A	N/A	81	1.05	0.3093
Fixed Effect: Oscillation number	N/A	N/A	243	113.52	<.0001
Fixed Effect: Group * Oscillation	N/A	N/A	243	5.16	0.0018
Novel L6 FS Cycle 1	-0.2047	0.2079	144.7	-0.98	0.3265
Novel L6 FS Cycle 2	0.1858	0.2079	144.7	0.89	0.3729
Novel L6 FS Cycle 3	0.2834	0.2079	144.7	1.36	0.1748
Novel L6 FS Cycle 4	0.4632	0.2079	144.7	2.23	0.0274
Novel L6 RS					
Fixed Effect: Genotype	N/A	N/A	427	0.22	0.6427
Fixed Effect: Oscillation number	N/A	N/A	1281	628.03	<.0001
Fixed Effect: Group * Oscillation	N/A	N/A	1281	7.19	<.0001
Novel L6 RS Cycle 1	-0.1812	0.06699	1040	-2.7	0.007
Novel L6 RS Cycle 2	0.1158	0.06699	1040	1.73	0.0841
Novel L6 RS Cycle 3	-0.07713	0.06699	1040	-1.15	0.2499
Novel L6 RS Cycle 4	0.04634	0.06699	1040	0.69	0.4893

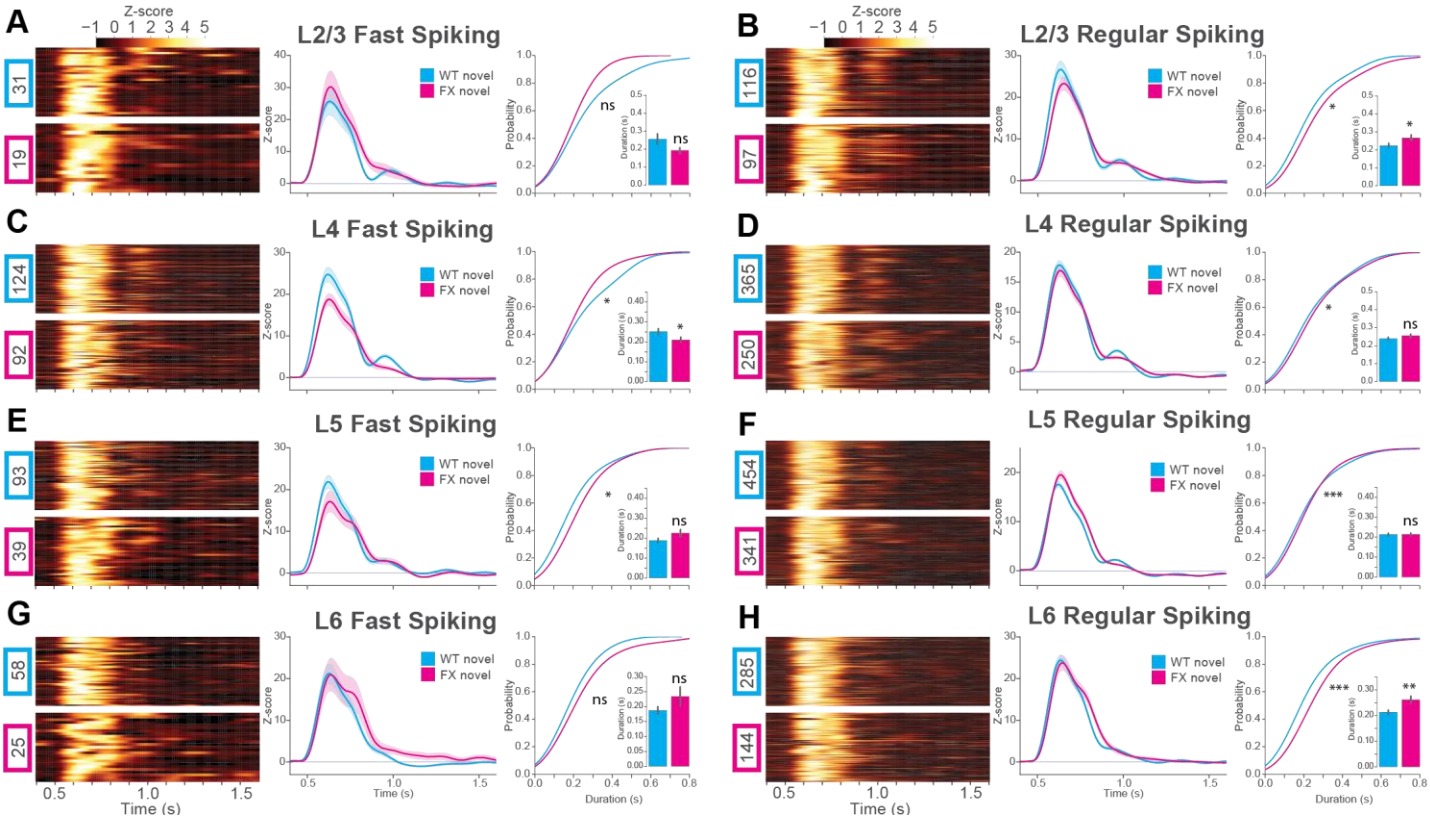

Figure S6. Responses to novel stimuli across all cortical layers and neural subtypes in WT and FX mice. Related to Figure 2.

Visually excited units in all layers in response to novel stimuli. WT (Cyan) 24 mice, FX (magenta) 18 mice. Z-scored firing rates are shown in the heatmaps. Population z-score line plots are shown to the right of the heatmaps. A cumulative distribution (CDF) of oscillation duration is shown to the right of the line plots, with bar graphs of the mean oscillation duration inset.

(A) L2/3 FS units: 2 sample KS test, novel WT vs FX duration: D(47)=0.22, p=0.58. Welch's t-test of mean duration: t(47)=1.82, p=0.07 (units after peak detection: WT pre N=31, FX pre N=18).

(B) L2/3 RS units: 2 sample KS test, novel WT vs FX duration: D(204)=0.20, p=0.02. Welch's unequal variances t-test of mean duration: t(204)=-2.13, p=0.03 (units after peak detection: WT pre N=112, FX pre N=94).

(C) L4 FS units: 2 sample KS test, novel WT vs FX duration: D(207)=0.22, p=0.01. Welch's t-test of mean duration: t(207)=2.14, p=0.03 (units after peak detection: WT pre N=121, FX pre N=88).

(D) L4 RS units: 2 sample KS test, novel WT vs FX duration: D(574)=0.13, p=0.01. Welch's t-test of mean duration: t(574)=-1.28, p=0.19 (units after peak detection: WT pre N=348, FX pre N=228).

(E) L5 FS units: 2 sample KS test, novel WT vs FX duration: D(124)=0.27, p=0.03. Welch's t-test of mean duration: t(124)=-1.61, p=0.11 (units after peak detection: WT pre N=90, FX pre N=36).

(F) L5 RS units: 2 sample KS test, novel WT vs FX duration: D(761)=0.16, p=3.58E-5. Welch's t-test of mean duration: t(761)=-0.12, p=0.89 (units after peak detection: WT pre N=435, FX pre N=328).

(G) L6 FS units: 2 sample KS test, novel WT vs FX duration: D(77)=0.21, p=0.42. Welch's unequal variances t-test of mean duration: t(77)=-1.32, p=0.19 (units after peak detection: WT pre N=57, FX pre N=22).

(H) L6 RS units: 2 sample KS test, novel WT vs FX duration: D(460)=0.26, p=5.43E-6. Welch's unequal variances t-test of mean duration: t(460)=-2.96, p=3.3E-3 (units after peak detection: WT pre N=278, FX pre N=184).

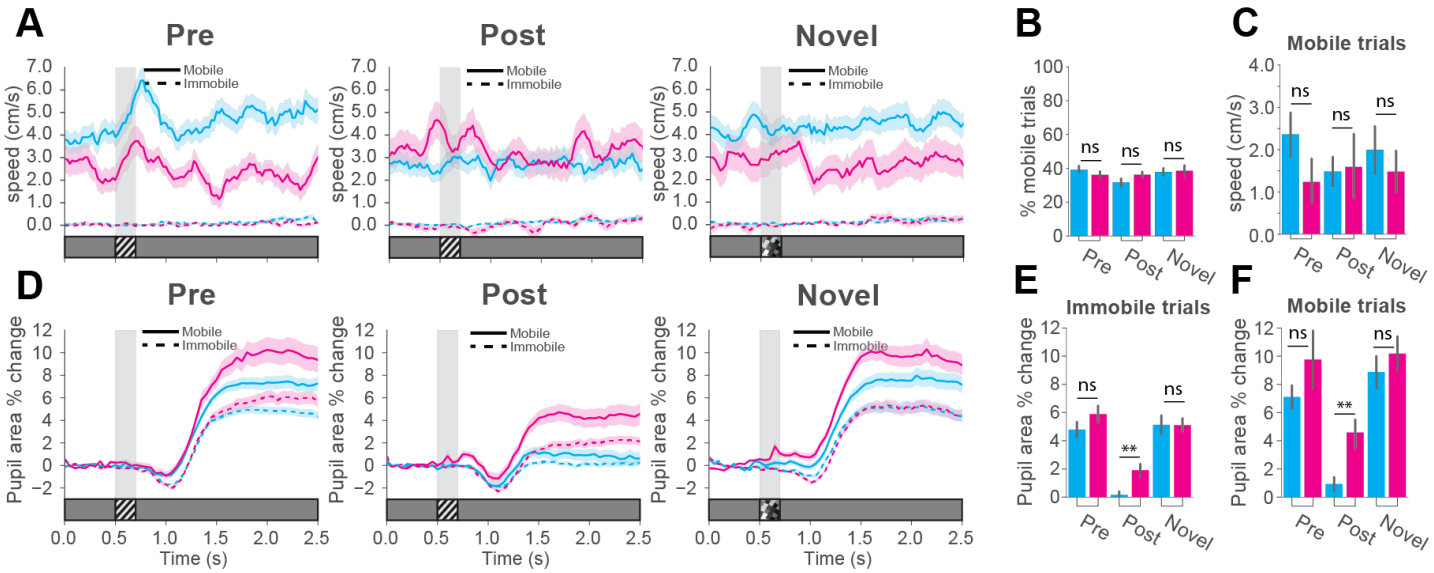

Figure S7. Locomotion and pupillometry. Related to Figures 1 and 2.

(A) Averaged locomotion traces for each recording condition (WT pre (cyan) = 20 mice, FX pre (magenta) = 12 mice, WT post (cyan) = 20 mice, FX post (magenta) = 12 mice, WT novel (cyan) = 20 mice, FX novel (magenta) = 11 mice. Only animals with both mobile and immobile trials are shown.

(B) Quantification of the percentage of mobile trials, averaged across mice for each stimulus condition. No significant differences could be found between WT and FX mice.

(C) Quantification of the mean speed across mice during the post stimulus response period (0.5 to 1.0 s) for mobile trials. T-test, WT pre vs FX pre: t(30)=1.86, p=0.07. WT post vs FX post: t(30)=-0.26, p=0.79. WT novel vs FX novel: t(29)=0.83, p=0.40.

(D) Pupillometry recordings, averaged and presented as pupil area percent change from the baseline period. WT pre (cyan)=34 mice immobile, 22 mobile. FX pre (magenta)=23 mice immobile, 11 mobile. WT post (cyan)=33 mice immobile, 14 mice mobile. FX post (magenta) = 23 mice immobile, 11 mobile. WT novel (cyan)=23 mice immobile, 17 mobile. FX novel (magenta)=16 mice immobile, 11 mice mobile.

(E) Quantification of the sustained surprise response period (1.5 s to 2.5 s) for each recording condition during immobile trials. Welch's t-test, WT pre vs FX pre :t(55)=-1.27, p=0.2. WT post vs FX post: t(54)=-3.33, p=2.04E-3. WT novel vs FX novel: t(37)=0.02, p=0.97.

(F) Quantification of the sustained surprise response period (1.5 s to 2.5 s) for each recording condition during mobile trials. Welch's t-test, WT pre vs FX pre :t(31)=-1.09, p=0.29. WT post vs FX post: t(23)=-3.00, p=9.10E-3. WT novel vs FX novel: t(26)=0.72, p=0.47.

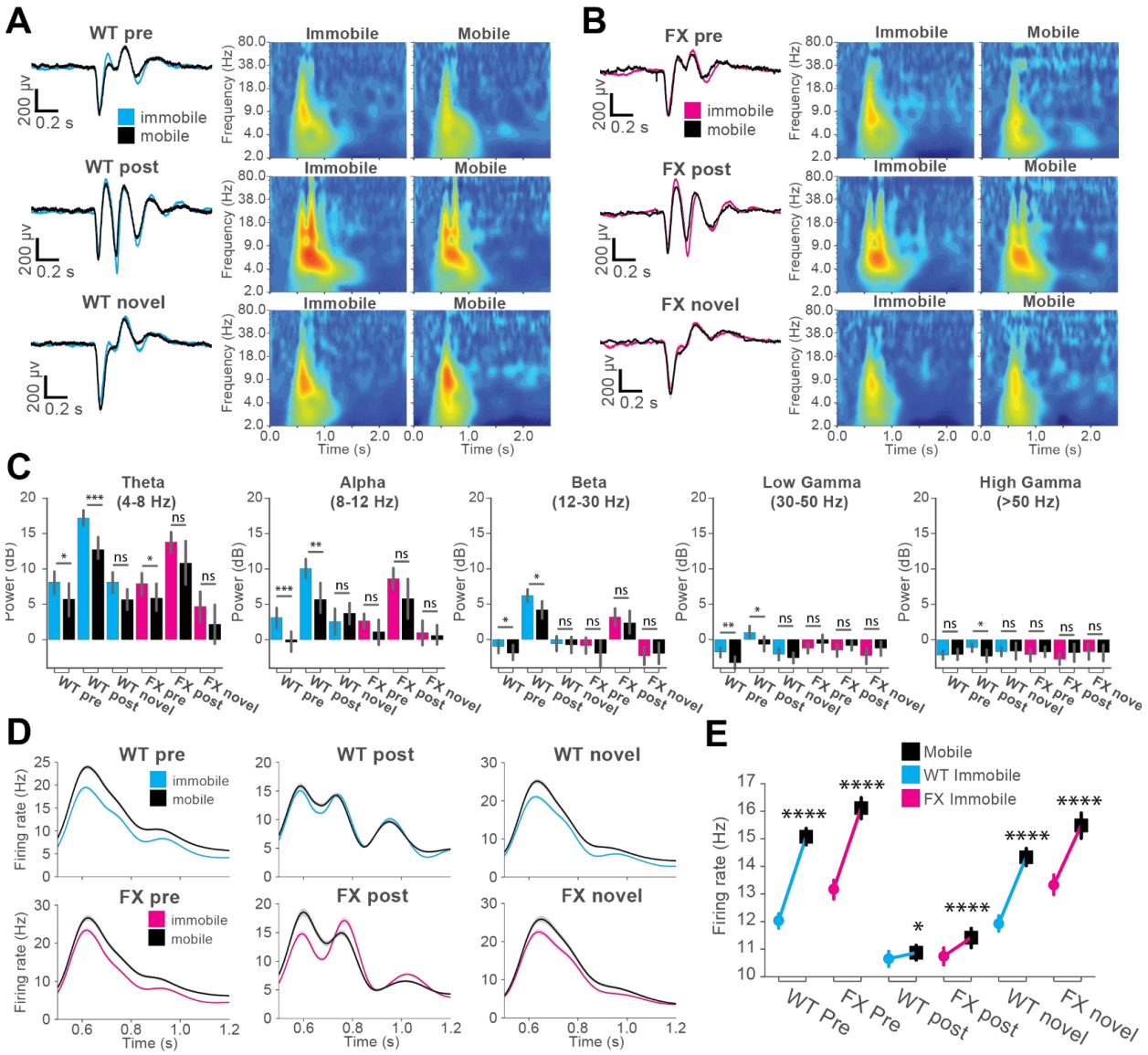

Figure S8. Locomotion decreases the power of low frequency oscillations while increasing firing rates. Related to Figures 1 and 2.

(A) Averaged time frequency spectrograms for WT mice during stationary trials (Cyan) or locomoting trials (black).

(B) Averaged time frequency spectrograms for FX mice during stationary trials (Magenta) or locomoting trials (black).

(C) Bar plots comparing the baseline normalized power between stationary and locomoting trials for each condition across different frequency bands. Mann-Whitney-U test, stationary vs locomoting Theta: WT pre: t=266, p=0.02. WT post: t=65, p=5.42E-5. WT novel: t=114, p=0.02. FX pre: t=84, p=0.01. FX post: t=154, p=0.06. FX novel: t=78, p=0.09.
Alpha: WT pre: t=172, p=2.37E-4. WT post: t=111, p=2.16E-3. WT novel: t=147, p=0.13. FX pre: t=111, p=0.07. FX post: t=155, p=0.06. FX novel: t=96, p=0.27. Beta: WT pre: t=284, p=0.04. WT post: t=136, p=0.01. WT novel: t=183, p=0.46. FX pre: t=126, p=0.15. FX post: t=175, p=0.15. FX novel: t=109, p=0.48. Low Gamma: WT pre: t=234, p=6.35E-3. WT post: t=143, p=0.01. WT novel: t=160, p=0.22. FX pre: t=127, p=0.16. FX post: t=174, p=0.14. FX novel: t=75, p=0.07.
High Gamma: WT pre: t=387, p=0.49. WT post: t=143, p=0.01. WT novel: t=184, p=0.47. FX pre: t=158, p=0.48. FX post: t=143, p=0.01. FX novel: t=184, p=0.47.

(D) Time courses of average firing rates from stationary or locomoting (black) trials for each condition.

(E) Mean firing rates from 0.5 to 1.0s from stationary or locomoting (black) trials for each condition. Only units with both mobile and immobile trials are compared against one another for each condition. A significant increase in firing rate is seen during locomotion for all conditions. Wilcoxon signed-rank test, WT pre, 1404 units : t=190957, p=5.12E-88. FX pre, 813 units: t=66902, p=5.37E-49. WT post, 724 units:, t=120176, p=0.04. FX post, 687 units: t=95999, p=2.04E-5. WT novel, 1188 units: t=165849, p=1.81E-56. FX novel, 757 units: t=67179, p=8.32E-37.

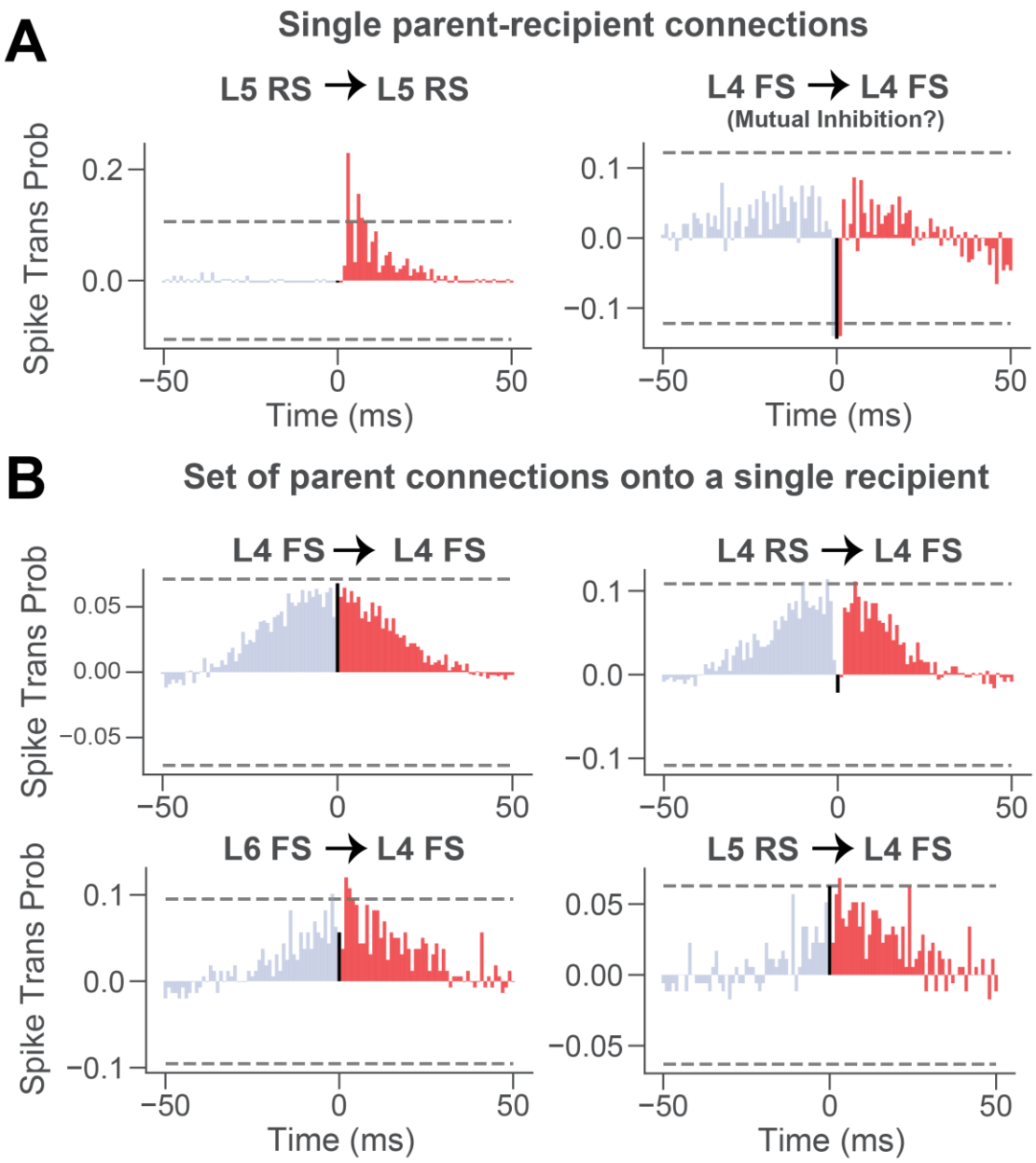

Figure S9. Example cross correlograms of unit pairs. Related to Figure 4.

(A) Example cross correlations of units from directed information analysis with single parent units sending information to single recipient units.

(B) Example cross correlations of units from directed information analysis where a set of 4 parents is predictive of the activity of a single recipient unit. Each correlation shown is between one of the 4 parents and the recipient unit.

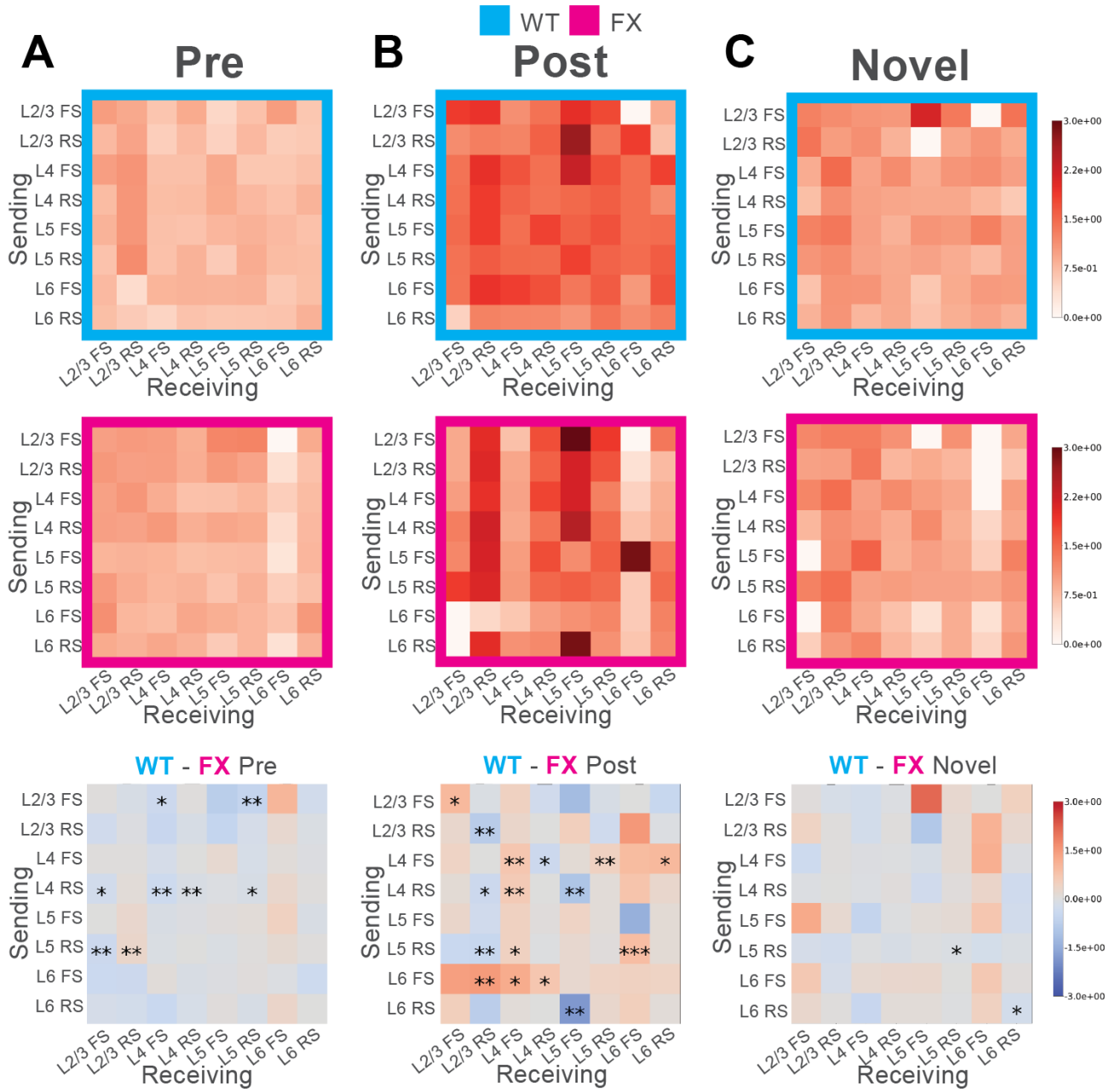

Figure S10. Layer and cell type specific changes in functional connectivity in WT and FX mice. Related to Figure 4.

(A) Functional connectivity (normalized directed information) pre perceptual experience for WT (Cyan) and FX (Magenta) mice, where a Markov order of 30 ms was used to compute directed information values. Darker colors indicate stronger (more predictive) connections. The vertical axis indicates cells in different layers sending information, while the horizontal axis indicates cells receiving that information. Bottom: difference between the WT and FX heatmaps. Monte Carlo simulations (10E6 runs) were used to approximate the permutation test for each square in each difference matrix above. Significance levels: '*' for $p<0.1$ and '**' for $p<0.05$ '***' for $p<0.01$.

(B) Functional connectivity post perceptual experience.

(C) Functional connectivity in response to novel stimuli.

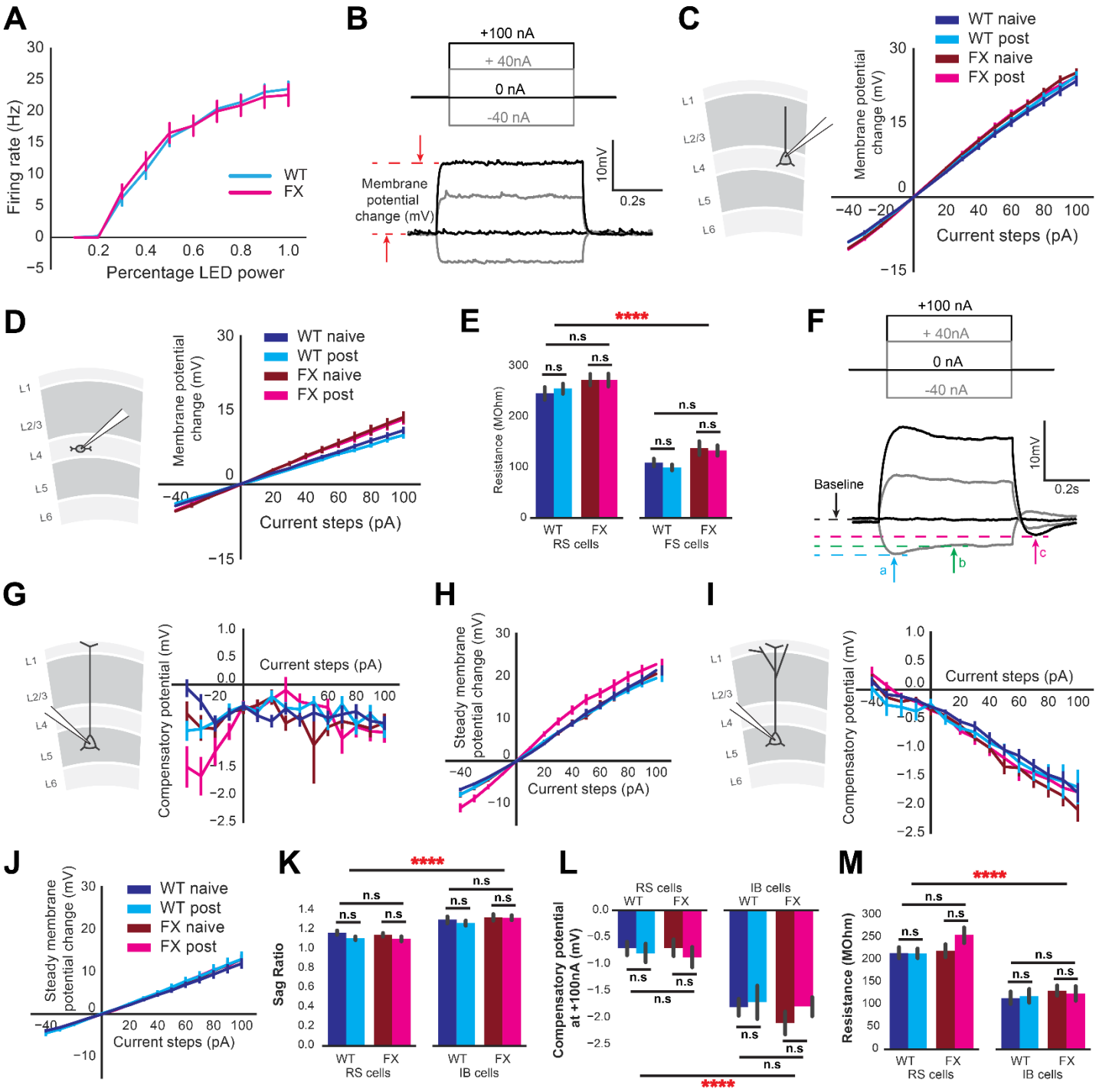

Figure S11. Characterizing layer 5 (L5) patched cell types. Related to Figures 5 and 6.

(A) ChR2-YFP positive L5 neurons in V1 were held under current clamp while full-field LED illumination was applied to measure the action potential frequency. N = 3 animals/21 neurons for WT and 4 animals/28 neurons for FX. Data reported in the curve are mean ± standard error of mean.

(B) Step current injection illustration and representative current-clamp traces from a layer 4 fast-spiking (FS) interneuron.

(C) Averaged current-voltage curve from L4 RS neurons showing the membrane potential change (demonstrated in A) at each current injection step.

(D) Averaged current-voltage curve from L4 FS interneurons showing the membrane potential change (demonstrated in A) at each current injection step.

(E) Mean input resistance for each group. Data reported in bar graphs are mean ± standard error of mean. Statistical significance on means was reported from three-way ANOVA followed by Tukey's HSD tests.

(F) Representative current-clamp traces from a layer 5 intrinsically-bursting (IB) neuron.

(G) Averaged compensatory current-voltage curve from L5 RS neurons showing the absence of rebound potential at the offset of step current injection.

(H) Averaged steady phase current-voltage curve from L5 RS neurons. The slope of the curves represents input resistance.

(I) Averaged compensatory current-voltage curve from L5 IB neurons showing the presence of rebound potential at the offset of step current injection (demonstrated in b).

(J) Averaged steady phase current-voltage curve from L5 IB neurons. The slop of the curves represents input resistance.

(K) Mean sag ratio (defined in B) for each group.

(L) Mean hyperpolarizing compensatory potential at the offset of +100nA current injection for each group.

(M) Mean input resistance for each group. Data reported in bar graph are mean ± standard error of mean. Statistical test on means was three-way ANOVA followed by multiple comparison test using Tukey's honest significant difference criterion.